PHYSICAL REVIEW B VOLUME 62, NUMBER 23 15 DECEMBER 2000-I

Theory of the electronic structure of GaN/AlN hexagonal quantum dots

A. D. Andreev* and E. P. O'Reilly
Department of Physics, University of Surrey, Guildford GU2 7XH, United Kingdom

(Received 25 January 2000; revised manuscript received 6 July 2000)

We present a theory of the electronic structure of GaN/AlN quantum dots (QD's), including built-in strain and electric-field effects. A Green's function technique is developed to calculate the three-dimensional (3D) strain distribution in semiconductor QD structures of arbitrary shape and of wurtzite (hexagonal) crystal symmetry. We derive an analytical expression for the Fourier transform of the QD strain tensor, valid for the case when the elastic constants of the QD and matrix materials are equal. A simple iteration procedure is described, which can treat differences in the elastic constants. An analytical formula is also derived for the Fourier transform of the built-in electrostatic potential, including the strain-induced piezoelectric contribution and a term associated with spontaneous polarization. The QD carrier spectra and wave functions are calculated using a plane-wave expansion method we have developed, and a multiband $\mathbf{k}\cdot\mathbf{P}$ model. The method used is very efficient, because the strain and built-in electric fields can be included analytically through their Fourier transforms. We consider in detail the case of GaN/AlN QD's in the shape of truncated hexagonal pyramids. We present the calculated 3D strain and electrostatic potential distributions, the carrier spectra, and wave functions in the QD's. Due to the strong built-in electric field, the holes are localized in the wetting layer just below the QD bottom, while electrons are pushed up to the pyramid top. Both also experience an additional lateral confinement due to the built-in field. We examine the influence of several key factors on the calculated confined state energies. Use of a one-band, effective-mass Hamiltonian overestimates the electron confinement energies by ~100 meV, because of conduction-band nonparabolicity effects. By contrast, a one-band valence Hamiltonian provides good agreement with the calculated multiband ground-state energy. Varying the QD shape has comparatively little effect on the calculated levels, because of the strong lateral built-in electric field. Overall, the transition energies depend most strongly on the assumed built-in electric field. The calculated variation of transition energy with quantum dot size is in good agreement with the available experimental data.

I. INTRODUCTION

Semiconductor quantum dots (QD's) have been of major interest in recent years. This has largely been stimulated by progress in QD growth technology, whereby self-organized, relatively uniform, dot layers can be achieved using the Stranski-Krastanow growth mode. Semiconductor QD's are of interest both from a fundamental physics perspective, enabling the study of zero-dimensional objects analogous to artificial atoms, and also because of potential device applications, particularly in the field of optoelectronics. Self-organized QD structures of relatively high quality have been successfully grown using a wide range of semiconductor compounds. These include III-V quantum dots based on GaAs,[1–3] InP,[4] GaSb,[5] and nitride structures,[6–9] as well as Group-II–VI (ZnSe-based[10,11]) Group-IV–VI (PbS-based),[12] and Si/Ge-based QD structures.[13] Nitride-based quantum dots have a special place in this list. Wide-bandgap nitride-based quantum well (QW) and dot structures have significantly different properties compared to the ''classical'' GaAs-based QW and QD structures. Whereas GaAs and most other Group-III–V compounds have a cubic (zincblende) crystal structure, GaN and related nitride alloys generally have a hexagonal (wurtzite) structure, which leads to strong built-in piezoelectric fields in heterostructures, of the order of MV/cm. As a consequence, self-organized GaN/AlN QD's can exhibit a large redshift in the energy of the photoluminescence maximum, with interband emission reported about 0.5 eV below the GaN bulk bandgap.[6] Moreover, unlike GaAs QD's, for which the electronic structure has been widely studied (see, e.g., Refs. 14–16 and references therein), the electronic structure of GaN/AlN QD's has not yet been theoretically analyzed in any detail.

Because of the rapid progress in QD growth technology, the theoretical study of self-organized QD's is now of major interest, both to interpret existing data, and also to guide future developments. A key requirement is for a relatively simple technique to reliably calculate the electron and hole energy levels and wave functions in any arbitrary-shaped QD structure. This is a considerably more difficult and computationally intensive task than for a quantum well structure, where quantization only occurs along one direction, and where Bloch's theorem can then still be used for the other two dimensions. The calculation of QD energy spectra must include the full three-dimensional quantization and the usually intricate shape of the QD's. In addition, it is necessary to determine the 3D distribution of the strain and piezoelectric fields, as a prerequisite to calculating the electronic structure of a QD. The real-space distribution of the strain and piezoelectric fields is generally found using finite-difference or atomistic techniques, which require substantial computational time and memory. The numerically determined strain distribution is then often Fourier transformed (numerically) into $\mathbf{k}$ space, in order to set up and solve the Hamiltonian matrix. We introduce here a method that considerably reduces this computational effort.

0163-1829/2000/62(23)/15851(20)/$15.00

The main aim of this paper is to study theoretically the electronic structure of hexagonal GaN/AlN QD structures and to compare the results with available experimental data. To the best of our knowledge, we present the first theoretical investigation of the carrier states in GaN-based QD's, which we carry out in the framework of a multiband $\mathbf{k}\cdot\mathbf{P}$ model, including the effects of the 3D strain and built-in electric-field distributions. We present an orginal technique based on a plane-wave expansion method to calculate the electron and hole energy spectra and wave functions. With this technique, we do not need to calculate explicitly the 3D distribution of the strain and built-in electric fields in real space. Instead, we can generate directly the Fourier transform of these distributions in $\mathbf{k}$ space, using analytical expressions which we have derived, and present below. The QD shape enters these expressions through the Fourier transform of its characteristic function, which can be derived analytically for a wide range of dot shapes. The proposed technique therefore provides a very convenient method to study the variation of the QD properties as a function of dot shape and size. The method used considerably reduces the computational effort compared to previous techniques, requiring that we calculate the carrier spectrum and wave functions of any QD structure by finding the eigenvalues and eigenvectors of a large matrix, all of whose elements are derived analytically. From a mathematical point of view, our method is therefore based on an efficient Fourier-transform technique.

The paper is organized as follows. In the next section we develop the method to calculate the 3D strain distribution in a QD of arbitrary shape. We derive an analytical expression for the Fourier transform of the strain tensor, and present results for the calculated spatial dependence of the strain tensor in GaN/AlN QD's shaped as truncated hexagonal pyramids and sitting on a wetting layer. We then derive, in Sec. III, analytical formulas for the Fourier transform of the built-in electrostatic potential, including the contribution due to the strain-induced piezoelectric field, and also due to the difference between the spontaneous polarizations of the QD and matrix materials. We demonstrate that, as previously found for quantum wells, both contributions are of similar magnitude in QD's. Section IV is devoted to the development of the plane-wave expansion method for calculating the carrier spectra and wave functions in QD structures using a multiband $\mathbf{k}\cdot\mathbf{P}$ model. We then present in Sec. V the calculated carrier spectra and wave functions for a range of GaN/AlN QD structures. We study the influence of the variation of QD shape on the carrier spectra, as well as the influence of nonparabolicity on the electron spectra, and of band mixing on the hole states in QD's. Section VI compares the calculated carrier spectra in QD's with the available experimental data from Ref. 6. We show that the calculated ground-state optical transition energy depends most strongly on the assumed difference between the spontaneous polarizations of bulk GaN and AlN. Using values in the range 0.032–0.052 C/m^2 for this polarization difference, we can obtain good agreement between the theoretical and experimental results. Finally we summarize our results and conclusions in Sec. VII.

II. STRAIN CALCULATIONS

The calculation of the spatial strain distribution in a QD structure requires the solution of a 3D problem in elasticity theory, often for a nontrivial quantum dot shape. This is often achieved using finite-difference methods or atomistic techniques.[14,17,18] These methods require considerable computational effort. A simple method to calculate the strain field in a semiconductor structure containing QD's of arbitrary shape was presented in Ref. 19 for the case when the elastic properties are assumed to be isotropic and the elastic constants of the QD and matrix materials are equal. The effects of anisotropic elastic constants on the strain distribution were included later in Refs. 20 and 21 for the case of a cubic (zinc-blende) crystal structure. We describe here the generalization of this approach to the case of hexagonal (wurtzite) crystals.

Consider a QD of arbitrary shape formed by embedding one kind of elastic material into a second elastic material with different lattice constants.[22] To keep the analysis as simple as possible, we consider here the case of equal elastic constants for the QD and matrix materials. The modification of the method to take account of different elastic constants in the dot and matrix is summarized in Appendix A. The displacement vector in a structure containing a single quantum dot can be expressed as the convolution of the Green's tensor, $G_{in}(\mathbf{r},\mathbf{r}')$, and the forces dF_n spread over the surface Ω' of the QD:

$$u_i(\mathbf{r})=u_i^{(0)}(\mathbf{r})+\int_{\Omega'}G_{in}(\mathbf{r},\mathbf{r}')dF_{\Omega}(\mathbf{r}'), \tag{1}$$

where the indices $i=1,2,3$ denote the three spatial directions, and $u_i^{(0)}$ is the displacement corresponding to any initial strain. When the elastic constants are equal in the QD and the matrix, the Green's tensor $G_{in}(\mathbf{r},\mathbf{r}')\equiv G_{in}(\mathbf{r}-\mathbf{r}')$, and satisfies the following equation:

$$\lambda_{iklm}\frac{\partial G_{\ln}(\mathbf{r})}{\partial x_k\,\partial x_m}=-\delta(\mathbf{r})\delta_{in}, \tag{2}$$

where λ_{iklm} is the elastic modulus tensor of the materials. In Eqs. (1) and (2), and below, we use the usual rule for summation over 1,2,3 for repeating indices unless the sum is indicated explicitly.

The surface force components dF_n in Eq. (1) can be expressed as $dF_n=\sigma_{nk}^T dS_k'$, where $\mathbf{S}'$ is a surface element at point r', with the associated normal vector directed outwards from the QD surface. We also use in Eq. (1) that $u_i^{(0)}(\mathbf{r})=u_i^T\chi_{\mathrm{QD}}(\mathbf{r})$ and $\sigma_{nk}^T=\lambda_{nkpr}e_{pr}^T$, where $\chi_{\mathrm{QD}}(\mathbf{r})$ is the characteristic function of the QD, equal to unity within the QD and zero outside, and $\sigma_{nk}^T,e_{pr}^T,u_i^T$ are components of the stress and strain tensors and the displacement caused by the "initial" strain due to the lattice mismatch between the QD and matrix materials.

For cubic and isotropic crystals we had for the initial strain that

$$e_{pr}^T=\frac{a_M-a_{\mathrm{QD}}}{a_{\mathrm{QD}}}\delta_{pr}\equiv\varepsilon_a\delta_{pr},$$

where a_M and a_{QD} are the elastic constants for the matrix and QD materials.[20,21] The situation is more complicated in a hexagonal crystal, where the tensor e_{pr}^T has the form

$$e^T_{pr} = \begin{pmatrix} \varepsilon_a & 0 & 0 \\ 0 & \varepsilon_a & 0 \\ 0 & 0 & \varepsilon_c \end{pmatrix} = \varepsilon_a \delta_{pr} + (\varepsilon_{ca}) \delta_{p3} \delta_{r3}, \tag{3}$$

with $\varepsilon_c = (c_M - c_{\mathrm{QD}})/c_{\mathrm{QD}}$ and $\varepsilon_{ca} = \varepsilon_c - \varepsilon_a$, the difference between the strain values along the *c* axis and the *a* axes. The displacement $u_i^S(\mathbf{r})$ due to a single QD of arbitrary shape embedded in an infinite matrix, is then given by

$$u_i^s(\mathbf{r}) = u_i^T \chi_{\mathrm{QD}}(\mathbf{r}) + \int G_{in}(\mathbf{r}-\mathbf{r}') \lambda_{nkpr} e^T_{pr}\, dS'_k. \tag{4}$$

Using Gauss's theorem and rewriting Eq. (4) in terms of the strain tensor rather than displacements, we obtain:

$$e^s_{ij}(\mathbf{r}) = e^T_{ij} \chi_{\mathrm{QD}}(r) + \frac{1}{2} \int_{\mathrm{QD}} \left[\frac{\partial G_{in}(\mathbf{r}-\mathbf{r}')}{\partial x_j \partial x_k} + \frac{\partial G_{jn}(\mathbf{r}-\mathbf{r}')}{\partial x_i\, \partial x_k} \right] \lambda_{nkpr} e^T_{pr}\, dV', \tag{5}$$

where integration is carried out over the QD volume. Using the convolution theorem and then taking the Fourier transform gives

$$\tilde{e}^s_{ij} = e^T_{ij} \tilde{\chi}_{\mathrm{QD}}(\xi) - \frac{(2\pi)^3}{2} \{ \xi_i \tilde{G}_{jn}(\xi) + \xi_j \tilde{G}_{in}(\xi) \} \times \lambda_{nkpr} \xi_k e^T_{pr} \tilde{\chi}_{\mathrm{QD}}(\xi). \tag{6}$$

Equation (6) gives the general expression for the Fourier transform of the strain tensor in a structure containing a single QD of arbitrary shape. This is a general formula valid for crystals of hexagonal or any other symmetry. Note that the QD shape enters only as the Fourier transform of the QD characteristic function.

For a hexagonal crystal the elastic modulus tensor λ_{iklm} has five independent components: $\lambda_{xxxx} = C_{11}$, $\lambda_{xxyy} = C_{12}$, $\lambda_{xxzz} = C_{13}$, $\lambda_{zzzz} = C_{33}$, and $\lambda_{yzyz} = C_{44}$, where C_{ij} are the elastic constants. A sixth component λ_{xyxy}, which one might at first expect to be independent, is related to these five by $\lambda_{xyxy} = \frac{1}{2}(C_{11} - C_{12})$. The elastic modulus tensor λ_{iklm} for a hexagonal crystal can also be expressed in a more general form in terms of the unit tensor δ_{ij}:

$$\begin{aligned} \lambda_{iklm} = {} & \alpha \delta_{ik} \delta_{lm} + \beta(\delta_{il}\delta_{km} + \delta_{im}\delta_{kl}) + \gamma \delta_{i3}\delta_{k3}\delta_{l3}\delta_{m3} \\ & + \kappa(\delta_{i3}\delta_{k3}\delta_{lm} + \delta_{ik}\delta_{l3}\delta_{m3}) + \rho(\delta_{im}\delta_{k3}\delta_{l3} \\ & + \delta_{i3}\delta_{m3}\delta_{kl} + \delta_{il}\delta_{k3}\delta_{m3} + \delta_{i3}\delta_{l3}\delta_{km}), \end{aligned} \tag{7}$$

where

$$\alpha = C_{12}, \quad \beta = \tfrac{1}{2}(C_{11} - C_{12}),$$

$$\gamma = C_{33} - 2C_{13} - 4C_{44} + C_{11},$$

$$\kappa = C_{13} - C_{12}, \quad \rho = C_{44} + \frac{C_{12} - C_{11}}{2}. \tag{8}$$

The first two terms in Eq. (7) correspond to the isotropic part, so the condition that the hexagonal crystal has isotropic elastic properties is that $\gamma = \kappa = \rho = 0$, i.e., the last three terms describe the elastic anisotropy of the hexagonal crystal. Using Eq. (7) and the expression for e^T_{pr} [Eq. (3)] we find

$$\lambda_{nkpr} e^T_{pr} = R \delta_{nk} + S \delta_{n3} \delta_{k3}, \tag{9}$$

where

$$R = (3\alpha + 2\beta + \kappa)\varepsilon_a + (\alpha + \kappa)\varepsilon_{ca}, \tag{10}$$

$$S = (\gamma + 3\kappa + 4\rho)\varepsilon_a + (2\beta + \gamma + \kappa + 4\rho)\varepsilon_{ca}. \tag{11}$$

Substituting Eq. (9) into Eq. (6) then gives

$$\begin{aligned} \tilde{e}^{(s)}_{ij} = \tilde{\chi}_{\mathrm{QD}}(\xi) \Big\{ & \varepsilon_a \delta_{ij} + \varepsilon_{ca} \delta_{i3} \delta_{j3} - \frac{(2\pi)^3}{2} R[\xi_i \xi_n \tilde{G}_{jn}(\boldsymbol{\xi}) \\ & + \xi_j \xi_n \tilde{G}_{in}(\boldsymbol{\xi})] - \frac{(2\pi)^3}{2} S[\xi_i \xi_3 \tilde{G}_{j3}(\boldsymbol{\xi}) + \xi_j \xi_3 \tilde{G}_{i3}(\boldsymbol{\xi})] \Big\}. \end{aligned} \tag{12}$$

The last step to derive an analytical formula for the Fourier transform $\tilde{e}^s_{ij}$ is to find the quantities $\tilde{G}_{j3}$ and the "scalar" products $\xi_n \tilde{G}_{jn} \equiv (\xi G)_j$. To do this we start from the Fourier transform of Eq. (2):

$$\lambda_{iklm} \xi_k \xi_m \tilde{G}_{ln}(\boldsymbol{\xi}) = \frac{\delta_{in}}{(2\pi)^3}. \tag{13}$$

Then with the help of the explicit expression for the tensor λ_{iklm} [Eq. (7)], we can rewrite Eq. (13) in the following form:

$$\begin{aligned} & (\beta \xi^2 + \rho \xi_3^2) \tilde{G}_{in} + [(\kappa + \rho) \xi_i \xi_3 + (\rho \xi^2 + \gamma \xi_3^2) \delta_{i3}] \tilde{G}_{3n} \\ & + [(\alpha + \beta) \xi_i + (\kappa + \rho) \delta_{i3} \xi_3](\xi G)_n = \frac{1}{(2\pi)^3} \delta_{in}. \end{aligned} \tag{14}$$

We derive from Eq. (14) two linear equations for G_{3n} and $(\xi G)_n$ and then solve the equations so obtained.[23] The first equation is found by rewriting Eq. (14) for $i = 3$:

$$P \xi_3 \tilde{G}_{3n} + I(\xi G)_n = \frac{\delta_{3n} \xi_n}{(2\pi)^3}, \tag{15}$$

where

$$P = (C_{33} - 2C_{44} - C_{13}) \xi_3^2 + C_{44} \xi^2, \tag{16}$$

$$I = (C_{13} + C_{44}) \xi_3^2. \tag{17}$$

To get the second equation for G_{3n} and $(\xi G)_n$ we multiply Eq. (14) by ξ_i and sum over *i* to find

$$Q \xi_3 \tilde{G}_{3n} + F(\xi G)_n = \frac{\xi_n}{(2\pi)^3}, \tag{18}$$

where

$$Q = (C_{33} - 2C_{13} - 4C_{44} + C_{11}) \xi_3^2 + (C_{13} + 2C_{44} - C_{11}) \xi^2, \tag{19}$$

$$F = (C_{13} + 2C_{44} - C_{11}) \xi_3^2 + C_{11} \xi^2. \tag{20}$$

Combining Eqs. (15) and (18) we solve the 2×2 linear system and find

$$\xi_3\tilde{G}_{3n}=\frac{1}{(2\pi)^3}\,\frac{1}{FP-IQ}\{F\delta_{3n}-I\}\xi_n, \tag{21}$$

$$(\xi G)_n=\frac{1}{(2\pi)^3}\,\frac{1}{FP-IQ}\{P-Q\delta_{3n}\}\xi_n. \tag{22}$$

Finally using Eqs. (21), (22), and (12), we obtain an analytical expression for the Fourier transform of the strain tensor for the case of hexagonal crystals:

$$\tilde{e}^s_{ij}=\tilde{\chi}_{\mathrm{QD}}(\boldsymbol{\xi})\left\{\varepsilon_a\delta_{ij}+\varepsilon_{ca}\delta_{i3}\delta_{j3}+\frac{RP-IS}{IQ-FP}\,\xi_i\xi_j\right.$$
$$\left.+\frac{SF-RQ}{IQ-FP}\,\xi_3\frac{\xi_i\delta_{j3}+\xi_j\delta_{i3}}{2}\right\}. \tag{23}$$

Although Eq. (23) provides an apparently complicated expression for the strain tensor, it is nevertheless straightforward to evaluate, with the expressions for P, I, Q, and F given by Eqs. (16), (17), (19), and (20); and the quantities R and S defined by Eqs. (10) and (11). It can also be shown that it reduces in the case of an isotropic crystal to the expression that we previously derived for $\tilde{e}^s_{ij}$, namely,

$$\tilde{e}^{\mathrm{iso}}_{ij}(\boldsymbol{\xi})=\varepsilon_0\tilde{\chi}_{\mathrm{QD}}(\boldsymbol{\xi})\left\{\delta_{ij}-\frac{3\lambda+2\mu}{\lambda+2\mu}\,\frac{\xi_i\xi_j}{\xi^2}\right\}, \tag{24}$$

where $\varepsilon_0\equiv\varepsilon_a\equiv\varepsilon_c$, and $\lambda=C_{12}$ and $\mu=C_{44}$ are the Lamé constants for an isotropic elastic medium.

The calculated elastic constant values for GaN and AlN[25] are such that the anisotropic elastic constant γ is of comparable magnitude to the isotropic elastic constants, α and β, while κ and ρ are about an order of magnitude smaller. We could therefore in principle set κ and ρ equal to zero in the strain distribution calculations. We choose however to keep them nonzero, and therefore to include the full anisotropy of the elastic constants in our strain calculations below.

The elastic problem is a linear one and so the solution for a periodic QD array is obtained as a superposition of the elastic fields for single QD's, namely,

$$e_{ij}=\sum_{n_1,n_2,n_3} e^s_{ij}(x_1-n_1d_1,x_2-n_2d_2,x_3-n_3d_3), \tag{25}$$

where d_1, d_2, and d_3 are the periods in the x, y, and z directions, respectively. If we assume a free-standing periodic array of dots, then an additional condition for e_{ij} arises from the requirement of minimum elastic energy for the periodic QD array. The strain tensor averaged over the elementary 3D superlattice unit cell is zero ($\overline{e_{ij}}=0$). From Eq. (25) it follows that the coefficients for the Fourier series expansion of e_{ij} are equal to $[(2\pi)^3/(d_1d_2d_3)]\tilde{e}^s_{ij}(\boldsymbol{\xi}_n)$, where $\boldsymbol{\xi}_n=2\pi(n_1/d_1,n_2/d_2,n_3/d_3)$. Finally, therefore, we obtain for the strain tensor in a free-standing QD array that

$$e_{ij}(\mathbf{r})=\frac{(2\pi)^3}{d_1d_2d_3}\sum_{n_1,n_2,n_3}\tilde{e}^s_{ij}(\xi_n)\exp(i\boldsymbol{\xi}_n\cdot\mathbf{r}), \tag{26}$$

where the summation is carried out over all values of n_1,n_2,n_3, with $\tilde{e}^s_{ij}=0$ when $n_1=n_2=n_3=0$. Thus, Eq. (26) when combined with Eq. (23) gives an analytical expression, in the form of a Fourier series, for the strain distribution in any free-standing structure of hexagonal symmetry that contains QD's of arbitrary shape.

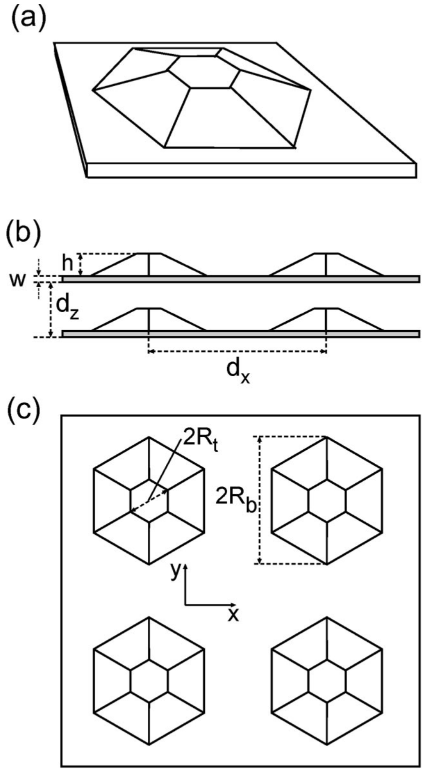

FIG. 1. Schematic diagrams of GaN/AlN QD's shaped as truncated hexagonal pyramids. (a) 3D view of a single QD standing on a wetting layer; (b) and (c) Views of the QD structure in the x-z and x-y planes, respectively. The QD size is determined by the diameters of the pyramid base and top, R_b and R_t (more precisely, these are the diameters of the circles that circumscribe the polygons at the bottom and the top), h is the QD height, and w is the thickness of the wetting layer. The QD's are modeled using a cubic superlattice with period $d_x=d_y$ in the growth plane and d_z in the growth direction.

The QD shape enters in Eq. (23) only in the form of the Fourier transform $\tilde{\chi}_{\mathrm{QD}}(\boldsymbol{\xi})$ of the QD characteristic function. Analytical expressions for $\tilde{\chi}_{\mathrm{QD}}(\boldsymbol{\xi})$ for different shapes (sphere, cube, cylinder, cone, square pyramid, truncated-square pyramid) are given in the Appendix of Ref. 20. The Fourier transform for a regular N-sided truncated pyramid is derived in Appendix B of this paper.

We now turn to apply Eq. (26) to investigate the strain distribution about GaN QD's embedded in an AlN matrix. A systematic high-resolution transmission electron microscope (HRTEM) analysis of this system[24] indicates that the dots form as truncated hexagonal pyramids standing on a thin wetting layer.[24] A schematic 3D view of one such QD is shown in Fig. 1(a) with cross sections shown in Figs. 1(b) (view in x-z plane) and 1(c) (view in x-y plane). In the calculations below, the shapes of the QD's are as presented in Fig. 1, with the sizes and vertical repeat distances used close to the experimental values.[24]

Figure 2 shows the calculated variation of the strain tensor components along the (0001) and $(01\overline{1}0)$ directions. For the (0001) direction [Fig. 2(a)], along the line through the pyramid center, the strain tensor components are of similar

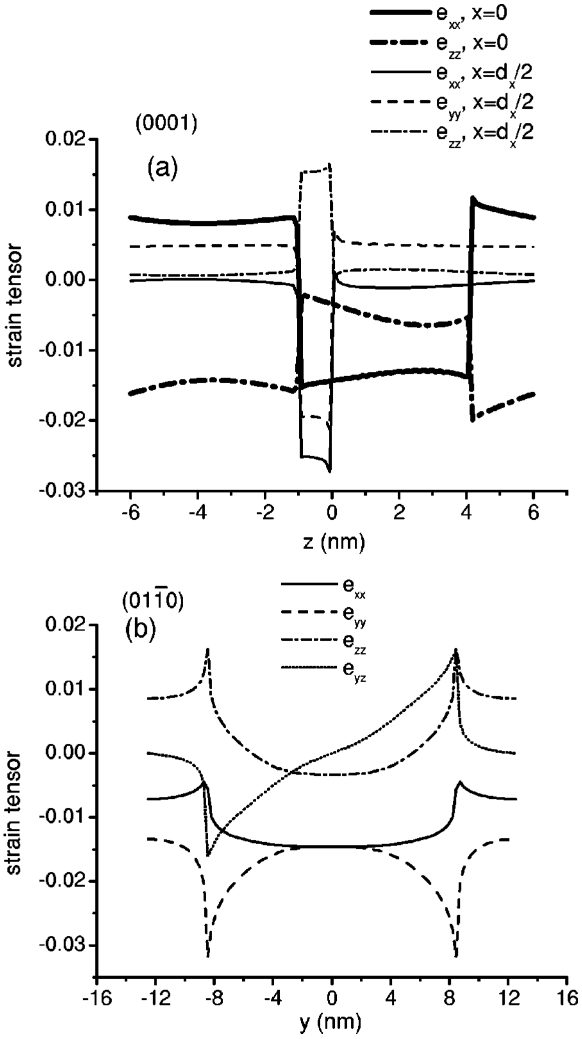

FIG. 2. Position dependence of the strain tensor components, calculated using Eq. (26) for the GaN/AlN QD structure shown in Fig. 1; (a) along the (0001) direction through the pyramid center ($x=y=0$, thick curves, for which $e_{xx}=e_{yy}$) and through the wetting layer between the pyramids ($y=0$, $x=d_x/2$, thin curves); (b) along the $(01\bar{1}0)$ direction, $x=z=0$. Material parameters used are listed in Table I. The dot dimensions are $R_b=8.5$ nm, $R_t=4$ nm, $h=4.1$ nm, $w=1$ nm, $d_x=d_y=25$ nm, and $d_z=12$ nm.

magnitude inside and outside the dot. This is because the GaN and AlN thicknesses (5.1 and 6.9 nm, respectively) are comparable along this line for the dot sizes considered here. Between the pyramids, and cutting through the wetting layer along the (0001) direction, the strain is much larger in the GaN wetting layer than in the AlN matrix. In addition, the magnitude of the biaxial strain component, $e_{zz}-1/2(e_{xx}+e_{yy})$ is much larger in the wetting layer than along the center of the dot, where e_{zz} is in fact negative, as would be found for a purely hydrostatic strain. Thus, the major part of the AlN matrix in the QD array is nearly unstrained since the fraction of the QD's in the total array volume is less than 10%. Turning to the $(01\bar{1}0)$ direction, Fig. 2(b) shows how the magnitudes of the strain fields peak near the pyramid edges, with smoother variations away from the edges.

The strain distribution in similar structures with smaller QD's ($h=2.8$ nm; total QD height, $h+w=3.3$ nm), was studied by HRTEM in Refs. 6 and 24. These studies deduced that the GaN dots are totally strained with respect to the AlN matrix. In addition, assuming uniform biaxial strain in the GaN QD, Arley *et al.*[24] managed to obtain good agreement between the simulated and measured interplanar distance profiles through the GaN dot. Therefore it was concluded in Ref. 24 that, to a first approximation, the strain distribution is uniform throughout each dot, with a value corresponding to the biaxial strain imposed by the surrounding AlN matrix. For these smaller QD's we have also calculated the strain distribution. Along the (0001) direction through the QD, the strain tensor components exhibit similar variations as those for large dots, which are presented in Fig. 2(a). However, for smaller dots the average strain value within the dot is larger, and the strain value also decreases more rapidly outside the dot. In particular, we found that $-e_{xx}\sim 1.7\%-2.1\%$ inside the dot, while e_{xx} decreases to $\sim 0.4\%$ between the dots. To a first approximation, these results agree with those of Ref. 24, where it was estimated that $e_{xx}\sim 0$ outside and $e_{xx}\sim 2.5\%$ inside the dot. It would be interesting to model the results of the HRTEM measurements of Ref. 24 using a more detailed simulation based on the predicted strain distribution about each dot, rather than just assuming a uniform biaxial strain model. Such an analysis is beyond the scope of the present paper. We note however that the model used in Ref. 24 is inconsistent with a range of calculations, all of which show that a single lattice-mismatched quantum dot introduced pseudomorphically into an infinite matrix material will always distort the material surrounding the dot.[14–16,19,20] In fact, this strain field outside the dot plays an important role in dot formation leading to the vertical correlation of the dots in the array. In such a vertically correlated QD array the strain fields from neighboring dots overlap outside the dots, so that nonzero strain tensor components must always exist in the matrix between the dots, as shown in Fig. 2(a), where e_{ii} is nonzero along the (0001) direction through the dots.

The strain distributions in Fig. 2 were determined using AlN elastic constant values in the dot and matrix regions. The elastic constant values were taken from a theoretical study by Wright[25] and are listed in Table I, along with the values calculated for GaN.[25] There are several reasons that justify using the same elastic constant values in the dot and matrix.[20] First, the elastic constants of GaN and AlN are relatively close to each other, as can be seen from Table I. Second, the calculated difference in the elastic constants of the two materials is less than the spread in values determined experimentally for GaN and AlN. For example, C_{11} equals 396 GPa for AlN and 367 GPa for GaN in Table I, while the experimentally reported values for AlN range from 345 GPa[27] to 411 GPa;[28] with GaN values ranging from 296 ± 18 GPa[29] to 390 ± 15 GPa.[30] A similar situation is found for the other elastic constants, so that the uncertainty in the elastic constant values partly justifies their being considered to be equal. Also, the elastic constants of a material in a state of high strain may differ from those for the unstrained bulk material, introducing further uncertainty as to the best choice of elastic constants. (Materials tend to get stiffer as they are compressed.) Related to this, Keyes[31] showed that, to a very good approximation, the elastic constants in most Group-III–V semiconductors depend chiefly on the nearest-neighbor lattice spacing. He proposed an empirical scaling rule, which has been supported by experimental data.[32] Ap-

TABLE I. Material parameters of bulk GaN and AlN used to calculate the strain and built-in electric fields. Elastic constants from Ref. 25; other parameters from Ref. 33.

Parameter	GaN	AlN
C_{11}, GPa	367	396
C_{12}, GPa	135	137
C_{13}, GPa	103	108
C_{33}, GPa	405	373
C_{44}, GPa	95	116
a, Å	3.189	3.112
c, Å	5.185	4.982
ϵ_{15}, C/m^2	-0.49	-0.6
ϵ_{31}, C/m^2	-0.49	-0.6
ϵ_{33}, C/m^2	0.73	1.46
P_{spont}, C/m^2	-0.029	-0.081
ϵ	9.6	9.6

plying this scaling rule to the case of QD's suggests that the most appropriate choice of QD elastic constants is to consider them equal to those of the matrix material.[20] We therefore assume equal elastic constants. For completeness, we also outline in Appendix A how the method introduced here can be adapted if required to take account of differing elastic constants in the dot and matrix materials.

In practice, the quantum dot arrays that have been studied experimentally, are not free standing but rather have been grown pseudomorphically on a thick buffer layer. In this case a different constraint is imposed on the strain components e_{ij}, due to the requirement to minimize the elastic energy in the whole structure (thick buffer and QD array), rather than only in the periodic QD array. We require that the strain tensor components averaged over the whole structure should be zero:

$$\int_{\text{buffer}} e_{ij}\, d^3\mathbf{r} + \int_{\text{QD array}} e_{ij}\, d^3\mathbf{r} = 0. \tag{27}$$

This equation provides the modified constraints necessary to determine the value of $\tilde{e}^s_{ij}(0,0,0)$. [We assume that the number of periods in the QD array is large enough so that the array can be considered as a QD superlattice and therefore Eq. (26) is still valid]. For a free-standing QD array, Eq. (27) requires $\tilde{e}^s_{ij}(0,0,0)=0$. However, if the thickness of the buffer layer is large enough, Eq. (27) then requires that the in-plane lattice constant of the QD array should be equal to that of the buffer. We can adapt Eq. (26) for this case simply by choosing values for $\tilde{e}^s_{ij}(0,0,0)$ such that the average in-plane lattice constant of the array equals that of the buffer, with the array then relaxing in the z direction due to the biaxial in-plane stress.[26] The GaN/AlN QD structures studied experimentally in Refs. 6 and 24 were grown coherently on a thick (1.5 μm) AlN buffer. For the ''large'' dots studied in Ref. 6 the QD's and wetting layer occupy a very small fraction of the total superlattice unit cell volume (2.4% and 4.1%, respectively, as we have used $d_x=d_y=30$ nm, $d_z=12$ nm, $w=0.5$ nm, $R_b=8.5$ nm, $R_t=2.1$ nm, and $h=3.6$ nm.) Therefore we can estimate the average strain in the QD array by replacing it with an $\text{Al}_{1-x}\text{Ga}_x\text{N}$ layer of equal average composition ($x=6.5\%$). The average strain $\tilde{e}^s_{ij}(0,0,0)$ in the QD array is then to a very good approximation equal to the uniform biaxial strain imposed by a thick AlN buffer on a thin $\text{Al}_{1-x}\text{Ga}_x\text{N}$ layer with $x=6.5\%$. Thus, due to the presence of the thick AlN buffer the average in-plane strain tensor components in the QD array differ from zero, with $e_{xx}=e_{yy}=0.16\%$. This value should have been used for $\tilde{e}^s_{xx,yy}(0,0,0)$ in Eq. (26), in order to take into account the presence of the thick AlN buffer on which the QD array was grown, with a correction of similar magnitude but opposite sign for $\tilde{e}^s_{zz}(0,0,0)$. This constant shift in the strain values is less than 10% of the characteristic strain values inside the dot. We neglect this shift in further calculations and consider free-standing QD arrays. The strain values for pseudomorphically strained layers can then be deduced from the figures shown here by adding a constant correction to the axial strain components.

III. DETERMINATION OF PIEZOELECTRIC FIELD AND POTENTIAL

It is by now well established that built-in piezoelectric fields significantly modify the electronic structure of GaN-based quantum wells (QW's) and heterostructures.[33] The effects are considerably stronger than those observed in cubic GaAs-based structures for several reasons. First, introduction of a uniform strain along the (0001) direction produces a nonzero piezoelectric field in nitride-based QW's, due to the symmetry of the wurtzite crystal structure. Second, the piezoelectric constants ϵ_{31} and ϵ_{33}, which determine the magnitude of the built-in field, are several times larger than the piezoelectric constant values found for GaAs and other Group-III–V binary compounds (see Table I and Ref. 33). In addition, the dimensions of a GaN or AlN unit cell differ slightly from those of an ideal hexagonal crystal. This small deviation introduces what is referred to as a spontaneous electrostatic polarization,[33] which also contributes to the built-in piezoelectric field. Although the effects of the piezoelectric potential have been widely studied in QW structures, we use the Fourier-transform method to introduce here what we believe is the first quantitative analysis of the variation in piezoelectric potential in a GaN-based QD structure.

We start with the Maxwell equation $\operatorname{div}\mathbf{D}=0$ for the displacement field $\mathbf{D}$, which is defined here by

$$\mathbf{D}=\varepsilon_r\mathbf{E}+4\pi(\mathbf{P}_{\text{strain}}+\mathbf{P}_{\text{spont}}), \tag{28}$$

where the strain-induced polarization, $\mathbf{P}_{\text{strain}}$ depends on the strain tensor e_{kl} as

$$P_i^{\text{strain}}(\mathbf{r})=\epsilon_{i,kl}e_{kl}=\epsilon^M_{i,kl}e_{kl}+\delta\epsilon_{i,kl}\chi_{\text{QD}}e_{kl}, \tag{29}$$

where $\epsilon^M_{i,kl}$ and $\epsilon^{\text{QD}}_{i,kl}$ are the piezoelectric constants for the matrix and dot materials, respectively, and $\delta\epsilon_{i,kl}=\epsilon^{\text{QD}}_{i,kl}-\epsilon^M_{i,kl}$. The spontaneous polarization contribution $\mathbf{P}_{\text{spont}}$, is directed along the c axis, and can be defined in terms of the characteristic function as

$$\mathbf{P}_{\text{spont}}(\mathbf{r})=\mathbf{P}^M_{\text{spont}}+[\mathbf{P}^{\text{QD}}_{\text{spont}}-\mathbf{P}^M_{\text{spont}}]\chi_{\text{QD}}(\mathbf{r}). \tag{30}$$

By taking the Fourier transform of the Maxwell equation $\operatorname{div}\mathbf{D}=0$ with $\mathbf{D}$ defined by Eq. (28), we find the Fourier transform of the built-in piezoelectric field $\mathbf{E}$,

$$\tilde{E}_i = -\frac{4\pi\xi_i\xi_l}{\varepsilon_r\xi^2}[\tilde{P}_l^{\text{spont}} + \tilde{P}_l^{\text{strain}}], \tag{31}$$

where the tilde denotes the Fourier transform. When using the Fourier transform technique to find the built-in electric field for a free-standing QD array, we include the additional condition that the electric field averaged over the unit cell of the QD superlattice is zero: $\overline{E_i} = 0$ (this follows from the requirement that the electric-field energy is minimized). This is achieved by requiring that $\tilde{E}_i$ is zero when ξ equals zero. The Fourier transform of the electrostatic potential φ, is related to the built-in electric field by $\tilde{\varphi} = -i\tilde{E}_i/\xi_i$. The Fourier transform of the piezoelectric potential is then made up of several contributions:

$$\tilde{\varphi} = \tilde{\varphi}^{\text{spont}} + \tilde{\varphi}^{\text{strain}} + \tilde{\varphi}^{\delta\epsilon}, \tag{32}$$

$$\tilde{\varphi}^{\text{spont}} = -i\frac{4\pi\xi_3}{\varepsilon_r\xi^2}(P_{\text{spont}}^{\text{QD}} - P_{\text{spont}}^{M})\tilde{\chi}_{\text{QD}}(\boldsymbol{\xi}), \tag{33}$$

$$\tilde{\varphi}^{\text{strain}} = -i\frac{4\pi}{\varepsilon_r\xi^2}[2(\xi_1\tilde{e}_{13} + \xi_2\tilde{e}_{23})\epsilon_{15} + \xi_3\epsilon_{31}(\tilde{e}_{11} + \tilde{e}_{22}) + \xi_3\epsilon_{33}\tilde{e}_{33}], \tag{34}$$

$$\tilde{\varphi}^{\delta\epsilon} = -i\frac{4\pi}{\varepsilon_r\xi^2}[2(\xi_1\tilde{e}_{13}^{\chi} + \xi_2\tilde{e}_{23}^{\chi})(\delta\epsilon)_{15} + \xi_3(\delta\epsilon)_{31}(\tilde{e}_{11}^{\chi} + \tilde{e}_{22}^{\chi}) + \xi_3(\delta\epsilon)_{33}\tilde{e}_{33}^{\chi}], \tag{35}$$

where $\tilde{e}_{ij}^{\chi}$ denotes the Fourier transform of the product $\chi_{\text{QD}}e_{ij}$ of the QD characteristic function and the elastic strain in the structure. The Fourier transform of the product is the convolution of the Fourier transforms of the individual terms, with $\tilde{e}_{ij}^{\chi}$ therefore given by

$$\tilde{e}_{ij}^{\chi}(\boldsymbol{\xi}) = \sum_{\tilde{\boldsymbol{\xi}}} \chi_{\text{QD}}(\boldsymbol{\xi} - \tilde{\boldsymbol{\xi}})\tilde{e}_{ij}(\tilde{\boldsymbol{\xi}}). \tag{36}$$

The first contribution to the electrostatic potential in Eq. (32) is due to the difference in the spontaneous polarizations of the QD and matrix materials. In deriving expression (33), we explicitly used that the spontaneous polarization is directed along (0001), i.e., $|\mathbf{P}_{\text{spont}}| \equiv P_3^{\text{spont}}$, as calculated by Bernardini *et al.*[33,34] and supported by several experiments.[35,36] The constant part $\mathbf{P}_{\text{spont}}^{M}$ of $\mathbf{P}_{\text{spont}}$ in Eq. (30) does not contribute to the potential because of the condition that $\varphi(\boldsymbol{\xi}=0)=0$. The second and third contributions to φ are due to the piezoelectric field associated with the strain distribution in the QD structure. The second term [Eq. (34)] describes the piezoelectric field when the piezoelectric constants of the QD and matrix are equal, while the third term [Eq. (35)] arises from any difference in these constants between the two materials. In deriving Eqs. (34) and (35) we use that for hexagonal Group-III–V crystals only the following components of the piezoelectric tensor are nonzero: $\epsilon_{1,13} = \epsilon_{2,23} = \epsilon_{15}$; $\epsilon_{3,11} = \epsilon_{3,22} = \epsilon_{31}$, and $\epsilon_{3,33} = \epsilon_{33}$.

Equations (33)–(35) give analytical formulas for the Fourier transform of the built-in electrostatic potential. These can be used directly to calculate QD carrier spectra and wave functions, as described in Sec. IV. However, we first apply them here to get an insight into the overall built-in potential, calculating the 3D distribution of the piezoelectric potential and of the electric field in the GaN/AlN QD structure shown in Fig. 1. For these calculations we summed a Fourier series similar to Eq. (25), with the substitution $e_{ij} \leftrightarrow \varphi$.

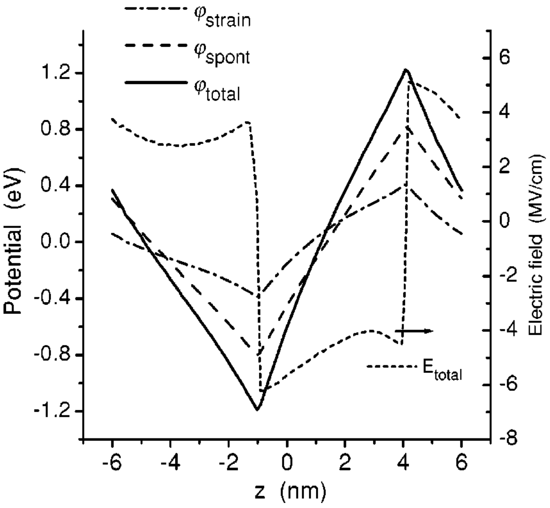

FIG. 3. Calculated variation of the built-in electrostatic potential components φ, and total electric field E, along the (0001) direction $(x=y=0)$, through the center of the pyramid shown in Fig. 2. Solid line: Total built-in electrostatic potential φ_{total}, found as the sum of the strain-induced piezoelectric potential, φ_{strain} (dot-dashed line) and the spontaneous polarization term φ_{spon} (dashed line). The dotted line shows the total built-in electric field. The material parameters used are listed in Table I.

Figure 3 shows the calculated variation of the total built-in electrostatic potential, φ_{total} (solid line), and electric field, E_z (dotted line) along the (0001) direction, through the pyramid center. The total potential is found as the sum of the strain-induced piezoelectric potential, φ_{strain} [dot-dashed line, given by Eqs. (34) and (35)], and the spontaneous polarization contribution, φ_{spon} [dashed line, from Eq. (33)]. Both contributions are of similar magnitude, and of the same sign. The magnitude of the electric field along the QD axis exceeds 6 MV/cm in the wetting layer, just below the pyramid. It decreases to about 4 MV/cm on moving from the pyramid base to the top. Outside the pyramid the electric field is around 4 MV/cm, but of opposite sign to that inside the QD. As with the strain field, the piezoelectric field is of similar magnitude inside and outside the pyramid, because the QD height plus wetting layer thickness is of the same order as the matrix thickness along this line. Along a (0001) line between the pyramids, the electric field is considerably larger in the GaN wetting layer than in the AlN matrix, because the wetting layer thickness is much smaller than the matrix thickness there ($w/d_z \ll 1$ in Fig. 1).

A giant built-in electric field of several MV/cm is characteristic of GaN/AlN structures and has been observed in several experiments. For example, a built-in electric field of 1 MV/cm was deduced from optical measurements on a GaN/Al$_x$Ga$_{1-x}$N QW structure with $x=0.27$.[36] In addition, the electric field was shown to depend linearly on the Al fraction x.[36] Therefore, it is natural to expect a built-in electric field of several MV/cm for $x=1$.

However, it should be noted that the calculated values of the built-in electric field depend strongly on the piezoelectric constants and on the spontaneous polarization values assumed for GaN and AlN. The values of these parameters used here are listed in Table I, and are taken from the work of Bernardini, Fiorentini, and Vanderbilt.[33] The piezoelectric constant ϵ_{15}, was not given in Ref. 33, so we have assumed it equal to ϵ_{31}, by analogy with other hexagonal crystals that exhibit strong piezoelectric properties. For ZnO and hexagonal CdS the piezoelectric constants ϵ_{15}, ϵ_{31}, and ϵ_{33} are -0.59, -0.61, and 1.14 and -0.21, -0.24, and 0.44, respectively (all in C/m^2).[37] These constants are of the same order as for GaN or AlN which we take to justify setting $\epsilon_{15}=\epsilon_{31}$ here. There remains however some uncertainty in the piezoelectric constants for GaN and AlN, and the spontaneous polarization values are also not known well, leading therefore to uncertainty in the calculated values of the built-in electric field in GaN/AlN QD's. We will return to discuss this point in more detail in Sec. VI of this paper.

Figure 4 presents a 2D contour plot of the calculated total electrostatic potential in the GaN/AlN QD of Fig. 3. The potential difference of over 2 V between the pyramid base and top creates a deep potential well for holes at the dot bottom and for electrons at the top. This is confirmed by Fig. 4(a), which shows a contour plot of the potential in the *x*-*z* plane $(y=0)$. The hole well is in fact deepest below the dot, in the wetting layer. Figure 4(b) shows the variation of the electrostatic potential in the wetting layer, at $z=-3w/4$, close to the deepest point in the hole well. The potential contours are nearly circularly symmetric, and therefore only weakly sensitive to the shape of the QD base. A similar result is observed for the electron well. Because the potential wells are also considerably wider in the wetting layer plane than in the growth direction, we will therefore analyze the symmetry of the electron and hole states in Sec. V by assuming the dots to have circular symmetry in the 2D growth plane.

The results presented in this section were obtained assuming a free-standing QD array. However, as already noted in the previous section, the structures studied experimentally in Refs. 6 and 24 were grown on a thick AlN buffer layer. The presence of this buffer layer introduces a nonzero average electric field into the QD array, pointing along the growth direction. Its magnitude can be estimated using a similar approach to that used for the strain field in the previous section. We estimate the value of this additional constant electric field by again replacing the QD array by an effective $\mathrm{Al}_{1-x}\mathrm{Ga}_x\mathrm{N}$ layer with $x=6.5\%$ (see Sec. III). We assume that the AlN buffer thickness is 1.5 μm and the QD array thickness is 0.24 μm, which corresponds to 20 periods of the QD superlattice in the growth direction.[6] When we impose the requirement that the electric field averaged through the complete structure is zero, we calculate that the piezoelectric and spontaneous-polarization induced electric fields are $E_{\mathrm{piezo}}=0.26\,\mathrm{MV/cm}$ and $E_{\mathrm{spont}}=0.32\,\mathrm{MV/cm}$ AlGaN (QD array) layer. This correction is about 10% of the total built-in electric field inside the dot. It is smaller than the uncertainty in the calculated value of the built-in electric field due to uncertainties in the piezoelectric constants and spontaneous polarization values. In addition, the field due to the buffer layer points entirely along the growth direction, and so causes no change to the variation in the lateral confinement potential for any fixed value of *z*, such as we considered in Fig. 4(b). We therefore ignore the influence of the buffer layer for the electronic structure calculations.

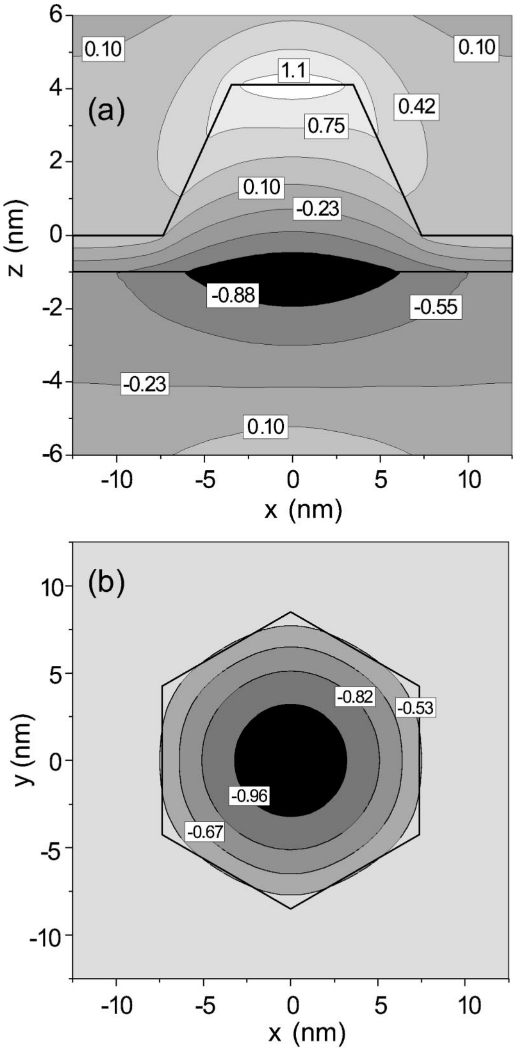

FIG. 4. Contour plots of the variation in the total built-in electrostatic potential, φ_{total}, for the QD's of Fig. 2, (a) in the *x*-*z* plane $(y=0)$, and (b) in the wetting layer at $z=-3w/4$. The darkest areas show regions of low potential (where holes are trapped), and the brighter areas regions of higher potential (where electrons are trapped). The numbers in boxes show the magnitude of the potential (in eV) along the different contour lines.

IV. PLANE-WAVE EXPANSION METHOD

We describe in this section our method to calculate the carrier spectrum and wave functions of QD structures, using the analytical expressions for the built-in strain and electric fields derived in the two previous sections.

The multiband envelope function approximation is widely used to calculate carrier spectra in semiconductor quantum structures. It has proved to be a convenient and reliable tool, describing well, e.g., the experimentally observed variation in interband transition energies due to quantum size effects in quantum well (QW) and QD structures.[38,39] In the envelope function method, the carrier states in a quantum structure are calculated by solving a Schrödinger-like equation with an effective multiband Hamiltonian, $\hat{\mathbf{H}}\Psi = E\Psi$. The number of bands included, N_H and the form of $\hat{\mathbf{H}}$ differ depending on the particular multiband Hamiltonian that is chosen. From a mathematical point of view the effective Hamiltonian equation describes a system of coupled differential equations. By using a plane-wave method, we can solve this system of equations using a Fourier-transform technique. From a physical point of view, this corresponds to describing the carrier states in terms of a linear combination of suitably chosen bulk states,[40] associated with a periodic array of bulk wave vectors. The effective Hamiltonian can then be naturally represented in the form

$$\hat{\mathbf{H}} = \hat{\mathbf{H}}_0 + \hat{\mathbf{V}}, \tag{37}$$

where the ‘‘perturbation’’ $\hat{\mathbf{V}}$ describes the difference between the potential in the quantum structure considered and the potential in the bulk Hamiltonian $\hat{\mathbf{H}}_0$ used for the basis states. The eigenstates of the bulk Hamiltonian are chosen as the basis states for the plane-wave expansion; each of these eigenstates then has the form

$$\Psi_{\mathbf{p},\mathbf{n},S}(\mathbf{r}) = \frac{1}{\sqrt{d_1 d_2 d_3}} \sum_{\alpha=1}^{N_H} B_\alpha^S(\mathbf{p},\mathbf{n}) u_\alpha(\mathbf{r}) \exp\{i[(\mathbf{p}_i - \boldsymbol{\xi}_\mathbf{n})\mathbf{r}]\}, \tag{38}$$

where $\alpha = 1, \ldots, N_H$ labels the basic Bloch functions $u_\alpha(\mathbf{r})$, $\mathbf{p}$ is the ‘‘quasimomentum’’ label for the 3D superlattice of quantum dots, $(\boldsymbol{\xi}_\mathbf{n})_i = 2\pi n_i/d_i$, $\mathbf{n}$ is the plane-wave number, and S denotes the different types of state included (e.g., doubly degenerate electron, heavy-, light-hole- and spin-split-off bands for $N_H = 8$). The operator matrix $\hat{\mathbf{V}}$ in Eq. (37) is obtained from the bulklike Hamiltonian by making the substitution $k_i \rightarrow -i\partial/\partial_i$, to take account of the spatial dependence of the band parameters. Details of the interface boundary conditions are included by an appropriate application of the differential operators at each interface. Each wave function of the effective Hamiltonian $\hat{\mathbf{H}}$ is then found as a series expansion with respect to the plane-wave states of Eq. (38):

$$\Psi_\mathbf{p}(\mathbf{r}) = \sum_S \sum_\mathbf{n} C_{\mathbf{p},\mathbf{n},S} \Psi_{\mathbf{p},\mathbf{n},S}(\mathbf{r}), \tag{39}$$

where the summation over S takes into account such effects as light- and heavy-hole mixing in heterostructures. The next step is to obtain the matrix $\mathbf{A}$, whose eigenvectors and eigenvalues are the coefficients $C_{\mathbf{p},\mathbf{n},S}$ and the energy spectrum of the QD. This matrix has the form

$$\begin{aligned} A_{i'i} &= E_S(\mathbf{p} - \boldsymbol{\xi}_\mathbf{n}) \delta_{S'S} \delta_{\mathbf{n}',\mathbf{n}} \\ &\quad + \sum_{\alpha'=1}^{N_H} \sum_{\alpha=1}^{N_H} [B_{\alpha'}^{i'}]^* B_\alpha^i \tilde{V}_{\alpha',\alpha}^{i'i}(\mathbf{n},\mathbf{n}'), \end{aligned} \tag{40}$$

where the numbers i' and i denote the set of quantum numbers $(\mathbf{p},\mathbf{n},S)$, $E_S(\mathbf{k})$ is the energy dispersion of the bulk state of type S, and $\tilde{V}_{\alpha',\alpha}(\mathbf{n},\mathbf{n}')$ is the Fourier transform of $V_{\alpha',\alpha}$:

$$\tilde{V}_{\alpha',\alpha}(\mathbf{n},\mathbf{n}') = \frac{1}{d_1 d_2 d_3} \int_{\Omega_0} e^{i\boldsymbol{\xi}_{\mathbf{n}'}\mathbf{r}} V_{\alpha',\alpha} e^{-i\boldsymbol{\xi}_\mathbf{n}\mathbf{r}} d^3 r. \tag{41}$$

The matrix elements $V_{\alpha',\alpha}$ depend *linearly* on the strain tensor components and on the built-in electric potential. Therefore the Fourier transform of $V_{\alpha',\alpha}$ is expressed through the Fourier transforms of the strain tensor, the built-in electrostatic potential, and the QD characteristic function χ_{QD}, introduced in the previous sections. Using a plane-wave expansion method in conjunction with the techniques introduced in previous sections, there is then no need to calculate the full spatial distribution of the strain and of the built-in electric field, unlike in other methods. This simple trick considerably reduces the computation time to set up calculations and makes the plane-wave method very effective for the further study of QD optical properties and modeling QD devices. We also note that the number of bulk states (‘‘plane waves’’) which must be included to obtain a given level of accuracy, is reduced in periodic structures with partly coupled QD’s. In addition, the maximum number of bulk plane-wave states, $N_i^{\max}$, which can be included along any direction *i*, in an envelope-function calculation, is less than the number of atomic layers in one period of the QD superlattice along that direction: $N_i^{\max} < d_i/a_i$. The envelope-function approximation is generally valid only when the envelope function varies smoothly over distances of the order of the lattice constant a_i. As a result, all terms with large wave vectors in the Fourier series $(k_i > 2\pi/a_i)$, should be neglected, since they must be negligibly small in the envelope-function approximation. This therefore provides an estimate for the maximum number of plane waves that should be included in the matrix expansion of Eq. (40). It also provides a means of testing the applicability of the plane-wave expansion method to calculate the carrier spectrum and wave functions in any given QD structure. If the number of plane waves required along a particular direction to calculate the wave function and carrier energy of a given level is less than the maximum number $N_i^{\max}$, then the plane-wave expansion method should be valid. This is because the terms in Eq. (40), which have large wave vectors $(k_i > 2\pi/a_i)$ and which should therefore be thrown away, do indeed make a negligibly small contribution to the solution of the Schrödinger-like equation $\hat{\mathbf{H}}\Psi = E\Psi$. We find for all the QD structures considered in this paper that the number of plane waves required along any direction is always much less than $N_i^{\max}$ and it is therefore appropriate to use the plane-wave expansion method.

We turn next to consider a suitable form of the multiband Hamiltonian for GaN/AlN QD structures. For hexagonal semiconductors, with wurtzite symmetry, the band structure near the energy gap can be well described using the Kane eight-band $\mathbf{k}\cdot\mathbf{P}$ Hamiltonian. A particularly characteristic feature of wurtzite GaN and AlN is their very small spin-orbit splitting values, Δ_{so}, of order 5–10 meV, compared to several hundred meV for most other Group-III–V and Group-II–VI semiconductors. To simplify the Hamiltonian, and reduce the size of the matrix in Eq. (40), we therefore neglect the spin-orbit splitting when calculating the electronic structure of GaN/AlN QD’s. This is justified because of the uncertainty in several other key parameters, including in particular the magnitude of the spontaneous polarization constants, P_{spont}, in GaN and AlN. We show later, in Sec. VI, how small changes in the assumed P_{spont} values significantly modify the calculated optical transition energies. By setting the spin-orbit splitting to zero instead of 5–10 meV, the 8×8 Hamiltonian decouples into two independent 4×4 Hamiltonians, one for spin-up and the other for spin-down states. Using as basis states $u_1=|S\uparrow\rangle$, $u_2=|(X+iY)\uparrow/\sqrt{2}\rangle$, $u_3=|(X-iY)\uparrow/\sqrt{2}\rangle$, and $u_4=|Z\uparrow\rangle$, the effective 4×4 Hamiltonian $\hat{\mathbf{H}}_0$ is then given by

$$\hat{\mathbf{H}}_0=\begin{pmatrix} E_g & \dfrac{P_\perp k_+}{\sqrt{2}} & \dfrac{P_\perp k_-}{\sqrt{2}} & P_\parallel k_z \\ \dfrac{P_\perp k_-}{\sqrt{2}} & F & K^* & -H^* \\ \dfrac{P_\perp k_+}{\sqrt{2}} & K & F & H \\ P_\parallel k_z & -H & H^* & \lambda \end{pmatrix}, \tag{42}$$

where

$$H=i\tilde{A}_6 k_z k_+ , \tag{43}$$

$$K=\tilde{A}_5(k_x^2-k_y^2+2ik_xk_y), \tag{44}$$

$$\lambda=-\Delta_1+\tilde{A}_1k_z^2+\tilde{A}_2(k_x^2+k_y^2), \tag{45}$$

$$\theta=\tilde{A}_3k_z^2+\tilde{A}_4(k_x^2+k_y^2), \tag{46}$$

$$F=\Delta_1+\lambda+\theta. \tag{47}$$

In the above equations, E_g and Δ_1 are the band-gap and crystal-field splitting of bulk GaN; $\tilde{A}_1$ to $\tilde{A}_6$ are the band parameters of GaN in the four-band model; the corresponding parameters A_1 to A_6 for a 3×3 valence-band Hamiltonian are given by the 3×3 lower corner of Eq. (42), and are presented in Table II in units of $\hbar^2/(2m_0)$ (where m_0 is the free-electron mass). The two sets of band parameters are related by

$$\tilde{A}_1=A_1+\frac{2m_0}{\hbar^2}\frac{P_\perp^2}{E_g},\quad \tilde{A}_2=A_2, \tag{48}$$

$$\tilde{A}_3=A_3-\frac{2m_0}{\hbar^2}\frac{P_\perp^2}{E_g},\quad \tilde{A}_4=A_4+\frac{m_0}{\hbar^2}\frac{P_\parallel^2}{E_g}, \tag{49}$$

$$\tilde{A}_5=A_5+\frac{m_0}{\hbar^2}\frac{P_\parallel^2}{E_g},\ \ \tilde{A}_6=A_6+\frac{\sqrt{2}m_0}{\hbar^2}\frac{P_\parallel P_\perp}{E_g}, \tag{50}$$

TABLE II. Band parameters of bulk GaN and AlN.

Parameter	GaN	AlN
E_g,[a] eV	3.5	6.3
Δ_1,[b] eV	0.022	−0.104
Δ_2,[b] eV	0.005	0.004
Δ_3,[b] eV	0.005	0.004
A_1	−7.24[c]	−4.17[a]
A_2	−0.51[c]	−0.58[a]
A_3	6.73[c]	3.68[a]
A_4	−3.36[c]	−2.17[a]
A_5	−3.35[c]	−2.27[a]
A_6	−4.72[c]	−2.21[a]
D_1, eV	0.7[d,e]	0.7[f]
D_2, eV	2.1[d]	2.1[f]
D_3, eV	1.4[d]	1.4[f]
D_4, eV	−0.7[d]	−0.7[f]
D_5, eV	−0.7[d]	−0.7[f]
D_6, eV	1.4[d]	1.4[f]
$m_\perp^c/m_0$[b]	0.20	0.33
$m_\parallel^c/m_0$[b]	0.18	0.25
a_c eV	−4.08[e]	−4.08[f]

[a] Reference 51.
[b] Reference 50.
[c] Reference 48.
[d] Reference 52.
[e] Reference 49.
[f] Assumed to be equal to that of GaN.

where $P_\perp$ and $P_\parallel$ are the momentum matrix elements of bulk GaN, related to the bulk electron effective masses $m_\perp$ and $m_\parallel$ by

$$P_\parallel^2=\frac{\hbar^2}{2m_0}\left(\frac{m_0}{m_e^\parallel}-1\right)\frac{(E_g+\Delta_1+\Delta_2)(E_g+2\Delta_2)-2\Delta_3^2}{E_g+2\Delta_2}, \tag{51}$$

$$P_\perp^2=\frac{\hbar^2}{2m_0}\left(\frac{m_0}{m_e^\perp}-1\right)\frac{\{(E_g+\Delta_1+\Delta_2)(E_g+2\Delta_2)-2\Delta_3^2\}E_g}{(E_g+\Delta_2)(E_g+\Delta_1+\Delta_2)-\Delta_3^2}. \tag{52}$$

In the above expressions for $P_\parallel$ and $P_\perp$, we allow for nonzero values of $\Delta_2=\Delta_{\text{so}}/3$ and Δ_3. This allows us to describe accurately the electron effective mass and conduction-band nonparabolicity in the four-band Hamiltonian, both of which are crucial to determining the electron-ground- and excited-state confinement energies.

The Fourier transform of the "perturbation" matrix $\tilde{V}_{\alpha',\alpha}$ in Eq. (41) is given by

$$\tilde{V}(\mathbf{n}',\mathbf{n})=\begin{pmatrix} \delta E_c & 0 & 0 & 0 \\ 0 & \delta F & \delta(K^*) & -\delta(H^*) \\ 0 & \delta K & \delta F & \delta H \\ 0 & -\delta H & \delta(H^*) & \delta\lambda \end{pmatrix}, \tag{53}$$

where

$$\delta E_c=U_c\tilde{\chi}_{\text{QD}}^{-}+a_c^{\text{QD}}(\tilde{e}_{11}+\tilde{e}_{22}+\tilde{e}_{33})-\tilde{\varphi}$$
$$+\delta a_c(\tilde{e}_{11}^{\chi^-}+\tilde{e}_{22}^{\chi^-}+\tilde{e}_{33}^{\chi^-}), \tag{54}$$

$$\delta F=\delta\Delta_1\tilde{\chi}_{\text{QD}}^{-}+\delta\lambda+\delta\theta, \tag{55}$$

$$\begin{aligned}\delta\lambda=&-U_v\tilde{\chi}_{\mathrm{QD}}^{-}+D_1^{\mathrm{QD}}\tilde{e}_{33}+D_2^{\mathrm{QD}}(\tilde{e}_{11}+\tilde{e}_{22})-\tilde{\varphi}+\delta D_1\tilde{e}_{33}^{\chi-}\\&+\delta D_2(\tilde{e}_{11}^{\chi-}+\tilde{e}_{22}^{\chi-})+[\delta A_1k_z'k_z+\delta A_2(k_x'k_x\\&+k_y'k_y)]\tilde{\chi}_{\mathrm{QD}}^{-},\end{aligned}\tag{56}$$

$$\begin{aligned}\delta\theta=&D_3^{\mathrm{QD}}\tilde{e}_{33}+D_4^{\mathrm{QD}}(\tilde{e}_{11}+\tilde{e}_{22})+\delta D_3\tilde{e}_{33}^{\chi-}+\delta D_4(\tilde{e}_{11}^{\chi-}+\tilde{e}_{22}^{\chi-})\\&+[\delta A_3k_z'k_z+\delta A_4(k_x'k_x+k_y'k_y)]\tilde{\chi}_{\mathrm{QD}}^{-},\end{aligned}\tag{57}$$

$$\begin{aligned}\delta K=&D_5^{\mathrm{QD}}(\tilde{e}_{11}+2i\tilde{e}_{12}-\tilde{e}_{22})+\delta D_5(\tilde{e}_{11}^{\chi-}+2i\tilde{e}_{12}^{\chi-}-\tilde{e}_{22}^{\chi-})\\&+\delta A_5(k_x'+ik_y')(k_x+ik_y)\tilde{\chi}_{\mathrm{QD}}^{-},\end{aligned}\tag{58}$$

$$\begin{aligned}\delta H=&D_5^{\mathrm{QD}}(\tilde{e}_{13}+i\tilde{e}_{23})+\delta D_6(\tilde{e}_{13}^{\chi-}+i\tilde{e}_{23}^{\chi-})\\&+\frac{\delta A_6}{2}[k_z'(k_x+ik_y)p_z(k_x'+ik_y')]\tilde{\chi}_{\mathrm{QD}}^{-},\end{aligned}\tag{59}$$

and where $\delta(K^*)$ and $\delta(H^*)$ are obtained from δK and δH [Eqs. (58) and (59)] by making the substitution $i\rightarrow -i$ (which is *not* the same as complex conjugation). In Eqs. (54)–(59), $\mathbf{k}=\mathbf{p}-\boldsymbol{\xi}_{\mathbf{n}}$ and $\mathbf{k}'=\mathbf{p}'-\boldsymbol{\xi}_{\mathbf{n}'}$ are the total quasimomenta; the Fourier transforms of quantities like $\tilde{\chi}_{\mathrm{QD}}^{-}$ and $\tilde{e}_{ij}$ are taken at $\boldsymbol{\tau}=\mathbf{n}-\mathbf{n}'$; $\tilde{e}_{12}^{\chi-}$ is the Fourier transform of the product $[1-\chi_{\mathrm{QD}}]e_{ij}$, which is given by convolution of $\tilde{e}_{ij}$ and $\tilde{\chi}_{\mathrm{QD}}^{-}$ [see Eq. (36)]; $\tilde{\chi}_{\mathrm{QD}}^{-}$ stands for the Fourier transform of $[1-\chi_{\mathrm{QD}}]$; U_c and U_v are the barrier heights for electrons and for holes at an *unstrained* GaN/AlN heterojunction; $\delta A_i=A_i^M-A_i^{\mathrm{QD}}$, $\delta D_i=D_i^M-D_i^{\mathrm{QD}}$, and $\delta\Delta_i=\Delta_i^M-\Delta_i^{\mathrm{QD}}$ are the material parameter differences. We emphasize that *all* terms in the above equations can be found analytically using the expressions for the Fourier transforms of the strain tensor $\tilde{e}_{ij}$ (given in Sec. II), and of the built-in electrostatic potential $\tilde{\varphi}$ (given in Sec. III). Thus, using the Fourier-transform technique, we have derived analytical expressions for all the elements of the main matrix A of Eq. (40), whose eigenvalues and eigenvectors are then the energies and wave functions of the carriers localized in the given QD structure.

The plane-wave expansion method developed above is also well suited to and has been successfully applied to calculate carrier spectra and wave functions in QD structures based on other material systems.[21,41,42] An expression for the Fourier transform of the strain tensor in a cubic crystal is derived in Ref. 20; while the piezoelectric potential in a cubic crystal is easily obtained using the method developed in Sec. III. The plane-wave expansion method is also very convenient for further modeling of the optical properties and laser gain characteristics of QD structures.[43,44] In contrast to other methods, where the carrier wave functions and optical matrix elements are found numerically in real space and then by numerical 3D integration, the plane-wave expansion method developed here allows the optical matrix elements to be expressed analytically through the coefficients $C_{\mathbf{p},\mathbf{n},S}$ [see Eq. (39)], which thereby considerably reduces the computation time, enabling more efficient modeling of QD laser characteristics.

V. NUMERICAL RESULTS

We present in this section the results of calculations of the carrier spectra and wave functions of electron and hole states in GaN/AlN QD's, including the influence on the results of the QD shape and of the Hamiltonian used in calculations.

The dot shapes and sizes are chosen to be close to the experimental data of Arley *et al.*,[24] and are as shown in Fig. 1. We take the dot and matrix compositions to be pure GaN and AlN, respectively, neglecting interdiffusion of Ga and Al atoms across the dot boundaries. This is consistent with the results of Arley *et al.*,[24] who used HRTEM and numerical simulations to determine the atomic interplanar distances across the GaN dots. The composition profiles were then fitted using a ''trial and error'' comparison between the experimental and simulated curves,[24] from which they concluded that there is no intermixing between Ga and Al in GaN dots. This contrasts with InAs/GaAs QD's, where strong intermixing has been observed.[41,45,46] We neglect in our calculations the relatively weak interdiffusion of Ga and Al atoms (0.15 monolayers) observed in the wetting layer between the dots, since, as we show below, the electrons and holes are strongly localized inside the dots and therefore the composition of the wetting layer outside the dot has negligible effect on these localized states. Thus, our assumption that the dot/matrix compositions are pure GaN/AlN is consistent with the existing experimental data.[6,24,47]

The dot base diameter $(2R_b)$ was observed to depend approximately linearly on dot height, h, in Ref. 47. We assume that the QD top diameter $(2R_t)$, also varies linearly with h. We calculate below the dependence of the carrier energy spectra in QD's on dot size, as we vary the QD height from $h=2$ nm to $h=4.1$ nm and the base and top diameters from $R_b=5.0$ nm to $R_b=8.5$; and $R_t=2$ and $R_t=4$ nm, respectively, consistent with the dot geometries of Ref. 47. The band-structure parameters that we use are listed in Table II.[48–52] There is some uncertainty in the published A_i values. For example, the published values of A_2 range from -0.51 (Ref. 48) to -0.91 (Ref. 49) for GaN and from -0.58 (Ref. 51) to -0.27 (Ref. 49) for AlN. There is less variation in the other A_i values. The values of the deformation potentials D_i and a_c are even less well-known than the A_i values. We could not find any published data for the D_i's and a_c in AlN; we therefore assumed them to be equal to those of GaN. There is also a wide spread in the published theoretical and experimental values for the valence-band discontinuity at AlN/GaN interfaces, with ΔE_v ranging from 0.5 (Refs. 53 and 54) to 1.4 eV.[55,56] Reference 54 also suggests that the valence-band discontinuity depends on the growth temperature. We use here the recent experimental value[54] of $\Delta E_v=0.5\pm 0.2$ eV. Because the strong built-in electric field creates very deep potential wells for electrons and holes (see Figs. 5 and 6), any uncertainty in the value of ΔE_v has much less effect on the calculated energy levels in GaN/AlN QD's than for other material systems. The greatest uncertainty in the calculated confined state energies arises from uncertainties in the values of the material parameters that determine the magnitude of the built-in electric field.

This is confirmed by Fig. 5, which shows the calculated variation of the conduction-band (CB) and heavy-hole valence band (VB) edges along the (0001) direction. The solid lines show the band-edge profiles through the pyramid center $(x=y=0)$, including both the strain deformation potentials and the built-in electrostatic potential of Fig. 3, while the dashed lines show the band-edge profiles with the electro-

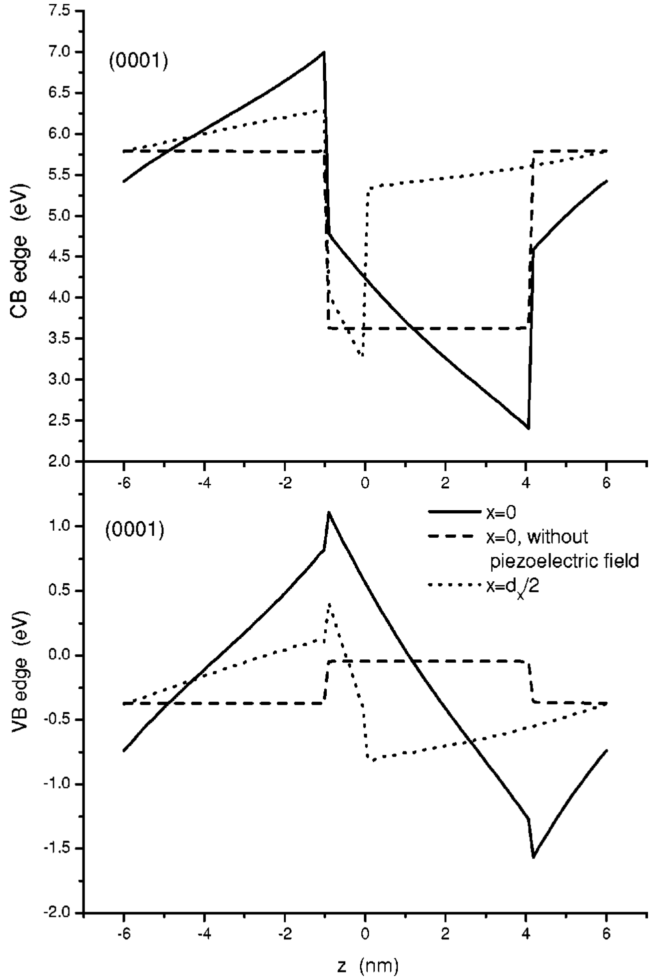

FIG. 5. Calculated variation of the conduction-band edge (CB, upper figure) and heavy-hole valence-band edges (VB, lower figure) along the (0001) direction for the QD's of Fig. 2. Solid lines: profiles through the pyramid center $(x=y=0)$, including the strain deformation potentials, and the built-in electrostatic potential of Fig. 3; for comparison, the dashed lines show the band-edge profiles, with the built-in electrostatic potential set to zero. Dotted lines: band edges along the (0001) direction through the wetting layer at $x=d_x/2$, $y=0$. Material parameters used are listed in Tables I and II.

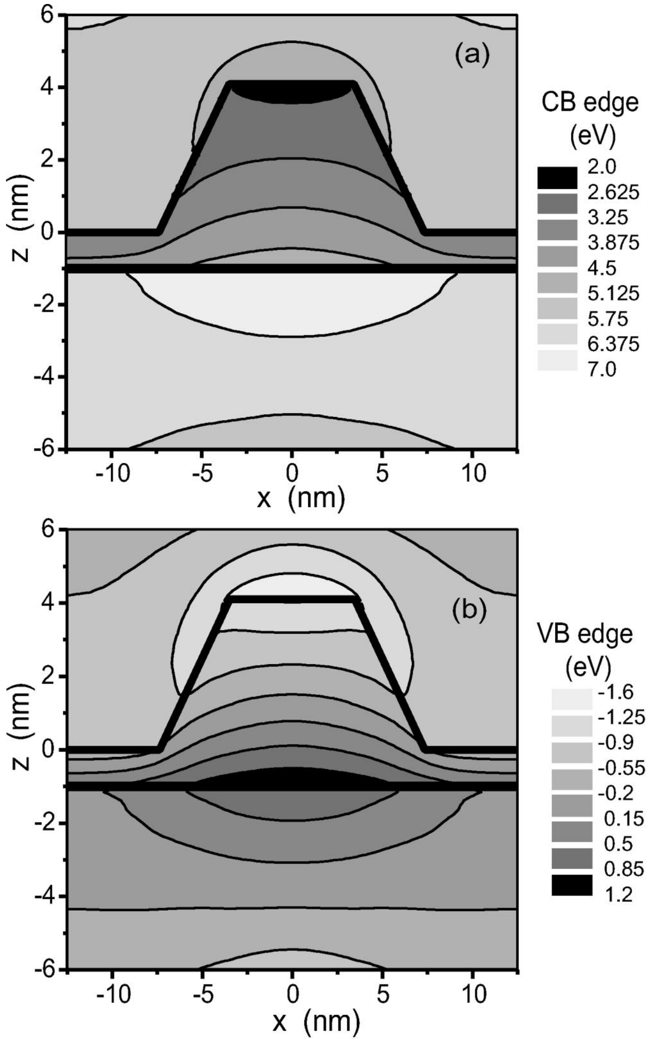

FIG. 6. Calculated 2D map of (a) the conduction-band (CB) edge, and (b) the valence-band (VB) edge for the GaN/AlN QD's of Fig. 2, including the strain deformation potentials and the built-in electrostatic potential. The darkest regions correspond to potential wells (a) for electrons in the upper figure, and (b) for holes in the lower figure. The boundaries between the QD or wetting layer and the matrix are indicated by thick-black lines.

static potential set to zero. This clearly demonstrates how the built-in electric fields crucially influence the carrier states in the QD. The electric field strongly separates the carriers; electrons are pushed up to the QD top and holes are pushed down into the wetting layer, below the pyramid base. The effect of the built-in potential is much stronger within the dots than in the wetting layer between the dots. The dotted line shows the variation of the band-edge profile along (0001) at $x=d_x/2$, $y=0$, from which it can be seen that the VB edge between the dots is 600 meV above the VB edge under the dot. The hole states therefore experience both a strong lateral and vertical confining potential due to the built-in fields, and are localized in the wetting layer, directly below the pyramid. The lateral confinement for holes, and for electrons, is confirmed by Fig. 6, which shows a contour plot of the calculated CB and VB profiles in the x-z plane $(y=0)$. These plots clearly illustrate that the electrons will be localized near the pyramid top [darkest region of Fig. 6(a)], and the holes in the wetting layer, just below the pyramid base [darkest region of Fig. 6(b)].

Figure 7 shows the probability density distribution, $|\Psi(\mathbf{r})|^2$, for the first five electron states in the hexagonal GaN/AlN QD of Fig. 2, calculated using the 4×4 Hamiltonian of Eq. (42). Because of the built-in electric field, the 3D potential well for the lowest electron states has roughly the shape of a short cylinder. We therefore analyze the electron states in the GaN/AlN QD by comparing them with those of an infinitely deep, cylindrical 3D potential well. The electron states in such a cylinder are characterized by three quantum numbers (n_z,n_r,m), where n_z is the quantum number along the cylinder axis z, n_r is the radial quantum number, and m is the z component of the angular momentum. In our case the cylinder is flat and we therefore need only consider states with $n_z=1$. States with $n_z=2,3,4,\ldots$ are at higher energy, as confirmed by Fig. 7, which shows that the first five states have only one maximum in the z direction, and are therefore $n_z=1$ states. The ground-state $E1$ is symmetric in the x-y plane, with $m=0$ and $n_r=0$ (see Fig. 7). This is followed by two almost degenerate states $E2$ and $E3$. These states would be degenerate in the flat cylinder, with $m=\pm 1$. The degenerate wave functions can be chosen to have a form similar to $E2$ and $E3$, with $\Psi_2 \propto \cos(\phi) J_1(k_{11} r)$ and $\Psi_3 \propto \sin(\phi) J_1(k_{11} r)$ (where J_m is the Bessel function of order m, whose nth root is given by Rk_{mn}, and with R the radius of the cylinder). The probability density of the second state E_2, has two maxima, at $\phi=0,\pi$, while $E3$ has two maxima, at $\phi=\pm\pi/2$ (see Fig. 7). The total probability density associated with the electrons in states $E2$ and $E3$ is then cylindrically symmetric, with $(|\Psi_2|^2+|\Psi_3|^2) \propto J_1^2(k_{11} r)$. Likewise, the wave functions calculated for $E4$ and $E5$ show them to be similar to states with $m=\pm 2$, which vary in the plane approximately as $\sin(2\phi)$ and $\cos(2\phi)$, respectively. The contour plot for $E5$ nevertheless clearly deviates from $\cos(2\phi)$ symmetry, as the lobes along the x axis have considerably smaller magnitude than those along the y axis. This reduction in the symmetry of the $E5$ state accounts for it being at a higher energy than $E4$, although the two states would be degenerate in a cylindrical potential. The wave functions and degeneracy of the first three electron states are then as expected for a cylindrical potential, due to the approximately circular symmetry of the lateral confinement due to the built-in electrostatic potential. However, the hexagonal symmetry of the dot in the x-y plane, and the cubic array of dots, which we have chosen, then become of greater importance for higher states, leading to the asymmetry of the $E5$ state, and the splitting of its degeneracy with the $E4$ state.

Figure 8 shows the probability density distribution, $|\Psi(\mathbf{r})|^2$ for the first five holes states in the hexagonal GaN/AlN QD of Fig. 2, calculated with the spin-orbit splitting set to zero, using a valence-band Hamiltonian H_v, based on the lower-right 3×3 part of the Hamiltonian matrix of Eq. (42), and with the parameters $\tilde{A}_i$ replaced by the A_i values. Usage of the full 4×4 Hamiltonian would have had little effect on the calculated results for the first five hole states. The valence-band basis states u_2 to u_4 used in Eq. (42) are quantized with respect to the (0001) direction, with angular momentum values of $+1$, -1, and 0, respectively, about the z axis. The band structure of bulk GaN along the (0001) direction can then be described in terms of three independent doubly degenerate bands, with $u_2=|(X+iY)\uparrow/\sqrt{2}\rangle$ and $u_3=|(X-iY)\uparrow/\sqrt{2}\rangle$ describing the heavy-hole spin-up (HH) bands, and $u_4=|Z\uparrow\rangle$ describing the light-hole spin-up (LH) band. There are, in addition, two further spin-down HH bands, and a spin-down LH band, which we do not need to consider. The calculated hole states can then be interpreted based on this 3×3 Hamiltonian, H_v. If we initially use a diagonal approximation to analyze the confined valence states [setting $K=H=0$ in Eq. (42)] then we can separately solve for each of the three valence bands in a flat, cylindrical potential, as was done for the electron states above. It can be seen from Figs. 4, 6, and 8 that the holes are considerably more tightly confined along the (0001) direction than within the plane of the wetting layer, so that again we need only consider states with $n_z=1$. Because the lattice constant of GaN is larger than that of AlN, the wetting layer is under biaxial compression, and so the light-hole (u_4) valence-band

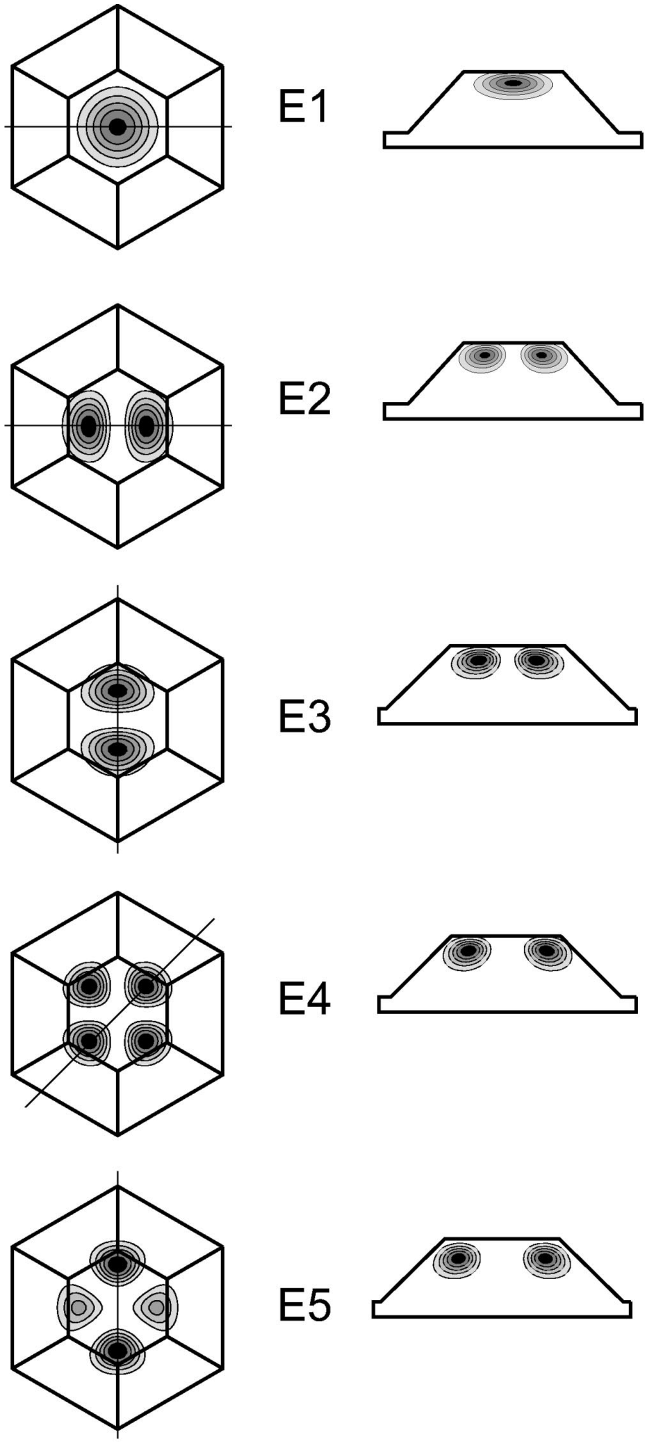

FIG. 7. Probability density distribution, $|\Psi(\mathbf{r})|^2$, for the five lowest electron states in the GaN/AlN QD of Fig. 2, calculated in the framework of an 8-band $\mathbf{k}\cdot\mathbf{P}$ model with zero spin-orbit splitting. The energies of the electron states are calculated, respectively, to be $E_1=3.020$ eV, $E_2=3.094$ eV, $E_3=3.095$ eV, $E_4=3.198$ eV, and $E_5=3.250$ eV (where $E=0$ corresponds to the unstrained bulk GaN valence-band edge). Darker areas indicate larger values of $|\Psi(\mathbf{r})|^2$. The left-hand plots show $|\Psi(\mathbf{r})|^2$ in the x-y plane at $z=3h/4$, while the right-hand plots show the cross section in a plane through the z axis and the thin line on the corresponding left-hand plot. Right-hand plots for $E1$ and $E2$ in the plane $y=0$, $E3$ and $E5$ for $x=0$, and $E4$ for the plane $x=y$. Material parameters used are listed in Tables I and II.

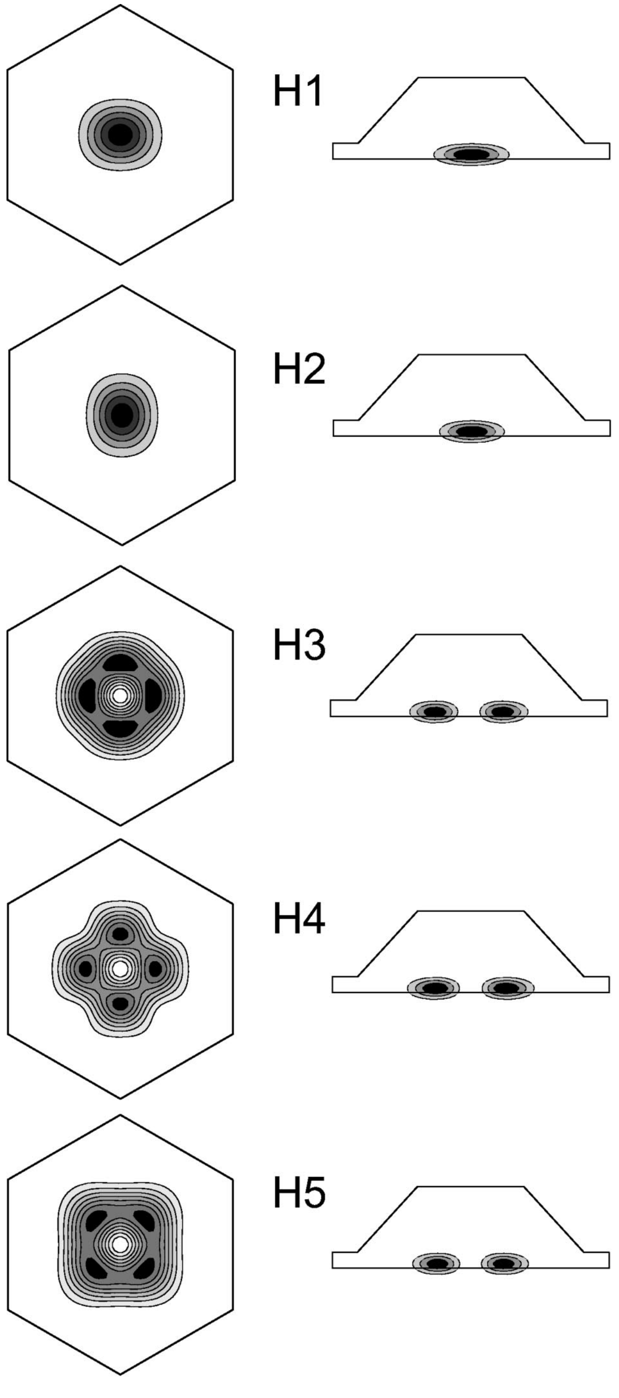

FIG. 8. Probability density distribution, $|\Psi(\mathbf{r})|^2$ for the first five hole states in the GaN/AlN QD of Fig. 2, calculated using a 3×3 Hamiltonian, with the spin-orbit splitting set to zero. The energies of the hole states are calculated, respectively, to be $E_1=E_2=0.726$ eV, $E_3=0.693$ eV, $E_4=0.671$ eV, and $E_5=0.662$ eV (where $E=0$ again corresponds to the unstrained bulk GaN valence-band edge). Darker areas correspond to larger values of $|\Psi(\mathbf{r})|^2$. The left-hand plots show $|\Psi(\mathbf{r})|^2$ in the x-y plane at $z=-w/2$, while the right-hand plots show a cross section in the x-z plane at $y=0$. Material parameters used are listed in Tables I and II.

energy is shifted down in energy compared to the heavy-hole band edges. In addition, the light-hole effective mass is considerably smaller than that of the heavy holes, so that the $n_z=1$ contribution to the light-hole confinement energy is considerably larger than that of the heavy holes. Both of these effects combine to shift the light-hole states well away from the valence-band edge.

The u_2 and u_3 states have the same diagonal matrix element F, in Eq. (42), so that in the diagonal approximation, each would therefore separately give a set of confined valence states with the same symmetry characteristics as the electron states, $E1$ to $E5$. When we now ''switch on'' the mixing between the three sets of valence bands, we find that the LH (u_4) states barely contribute to the band-edge valence states. The mixing between the u_2 and u_3 states gives rise to a doubly degenerate ground state, for which the two states $H1$ and $H2$ have wave functions that are found in Fig. 8 to be slightly prolate along the x and y directions [although their combined probability density, $(|\Psi_1|^2+|\Psi_2|^2)$, is to a good approximation circularly symmetric]. The off-diagonal matrix element K, mixes u_2 states with angular momentum component m with u_3 states with component $(m+2)$. This then qualitatively changes the character of the excited valence states ($H3$ to $H5$ in Fig. 8), so that $H3$ for instance has four probability density lobes in the x-y plane, rather than the two lobes observed for each of the doubly degenerate $E2$ and $E3$ states.

Electronic structure calculations become considerably simpler if a multiband effective Hamiltonian can be replaced by a one-band model to calculate electron and hole confined state energies in QW or QD structures. We therefore turn now to investigate the validity of using a one-band Hamiltonian to determine electron and hole confined state energies in GaN/AlN QD's.

The one-band effective-mass Hamiltonians for electrons and heavy holes are assumed, respectively, to have the form

$$H^{1\times1}_{\mathrm{elec}}=U_c\chi^{-}_{\mathrm{QD}}+\frac{\hbar^2}{2}\left[k_x\frac{1}{m_c^{\parallel}}k_c+k_y\frac{1}{m_c^{\parallel}}k_y+k_z\frac{1}{m_c^{\perp}}k_z\right]+a_c(e_{xx}+e_{yy}+e_{zz})-\varphi \tag{60}$$

and

$$H^{1\times1}_{\mathrm{hole}}=-U_v\chi^{-}_{\mathrm{QD}}+(A_1+A_3)k_z^2+(A_2+A_4-A_5)(k_x^2+k_y^2)+(D_1+D_3)e_{zz}+(D_2+D_4-D_5)(e_{xx}+e_{yy})-\varphi, \tag{61}$$

where all the Hamiltonian parameters have been defined earlier. The one-band energy spectrum calculations were carried out using the same method as described in the previous section, namely, using Eqs. (37)–(41), which are valid for an arbitrary Hamiltonian of any size.

Figure 9 shows the variation of (a) electron and (b) hole confined state energy, as a function of dot size, calculated using an appropriate multiband Hamiltonian (solid lines), and the one-band, effective-mass Hamiltonians of Eqs. (60) and (61). We see from Fig. 9(a) that the difference between the results of the one-band and four-band model is around 100 meV for the ground electron level $E1$ in the smallest (2 nm) dot considered, and decreases only slightly to about 70 meV for the 4 nm dot. The calculated differences are even larger for the higher levels $E2, E3, E4, \ldots$.

This result is initially very surprising. The one-band model assumes the conduction-band dispersion to be parabolic, and has been shown to give a generally accurate esti-

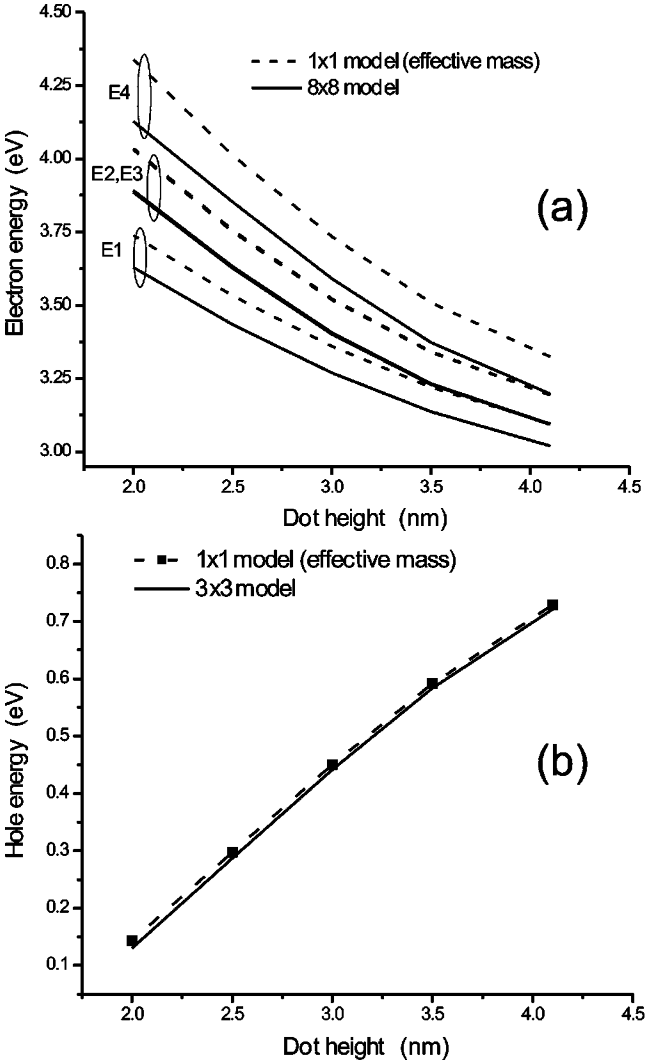

FIG. 9. Variation of (a) the electron and (b) hole energy levels as a function of QD height, calculated using different models for the bulk band structure. Solid lines: energies calculated using a four-band model for electrons (three-band model for holes), each with the spin-orbit interaction set to zero. Dashed lines: energies calculated using one-band effective-mass models. The zero of energy is set at the VB edge of bulk unstrained GaN. Material parameters used are listed in Tables I and II. The dot geometry varies with QD height as described in the text.

mate of the ground-state confinement energy, e.g., in GaAs/AlGaAs quantum well structures,[57,58] even for large confinement energies, where nonparabolicity effects are becoming important. For a bulk semiconductor, the relative deviation between the electron energies at fixed k in the 1×1 and 4×4 models is of order $\Delta E/E_g$, where ΔE is measured from the conduction-band (CB) edge. A similar estimate can also be applied for the QD case. In wide-band gap semiconductors such as GaN, the effect of nonparabolicity on the electron energy is therefore weaker than in narrower gap semiconductors like GaAs or even InAs, so we might expect that nonparabolicity effects should be negligible in the GaN QD's, particularly as the electron ground-state energy in the 2 nm dot is at 3.6 eV, close to the bulk GaN conduction-band-edge energy of 3.5 eV. However, the zero of energy in Fig. 9 is set at the valence-band edge of bulk, unstrained GaN, and the built-in electric field causes the conduction-band-edge energy to vary rapidly with position through the QD. The energy shift ΔE counted from the CB edge then varies strongly as we move from the QD center ($\Delta E \sim 0$) to the top of the pyramid where $\Delta E \sim 700\,\text{meV}$ (see the band-edge profile in Fig. 5). Most of the electron wave function is localized near the top of the pyramid, so that the average value of ΔE is then large. As a result, the conduction-band nonparabolicity has a marked effect on the calculated electron energy levels in GaN/AlN QD's [see Fig. 9(a)].

Similar effects for holes should be much weaker, because the hole confinement along the (0001) direction is determined primarily by the heavy-hole effective mass. The heavy-hole dispersion remains parabolic to larger wave vectors, and the larger mass also leads to the heavy-hole having a tighter vertical confinement. Figure 9(b) shows that the one-band heavy-hole Hamiltonian of Eq. (61) can be successfully applied to predict approximately the same hole ground-state energy as is obtained using the 3×3 valence Hamiltonian based on Eq. (42).

All the calculations presented above were for hexagonal QD's, shaped as in Fig. 1. Such a shape is consistent with the underlying crystal symmetry, and also with the hexagonal symmetry observed in the dot reflection high-energy electron diffraction pattern by Arley *et al.*[24] However, it remains a complex problem to completely determine the QD shape from experiment. The high-resolution TEM studies carried out for instance in Ref. 24 probe a vertical dot cross section, thereby giving values for the bottom and top radii R_b and R_t, and the width w of the wetting layer. HRTEM does not directly confirm the dot shape. To study the effect of a change in QD shape on the energy spectra, we have therefore considered 4-sided, 6-sided, and 20-sided regular truncated pyramids, and calculated the electron and hole energy levels in each case as a function of dot size. The 20-sided pyramid is included to model a truncated conical structure. We can change the QD shape by varying just one parameter in the calculation, namely, the number of corners N_{corner} entering in the Fourier transform of the QD characteristic function (see Appendix B). We kept the bottom and top sizes R_b and R_t, fixed for a given dot height. Figure 10 shows the calculated dependence of the QD ground-state energy levels on size for the three different dot shapes. The variation of the QD shape shifts the electron and hole energies, but does not change qualitatively the structure of the wave functions, which remain similar to those of Figs. 7 and 8. The energy levels in the hexagonal ($N_{\text{corner}}=6$) and conelike QD's ($N_{\text{corner}}=20$) are very close to each other, differing by only about 20 meV; the volume of the square-based pyramid ($N_{\text{corner}}=4$) is significantly less than for the two other shapes and therefore the electron and hole ground levels are ~60–100 meV higher and lower, respectively, than in the hexagonal and conelike structures (see Fig. 10). Nevertheless, as shown in the next section, the uncertainty in the QD energy states due to any uncertainty in the dot shape, is much smaller than that due to the uncertainty in the material parameters that determine the magnitude of the built-in electric field.

VI. COMPARISON WITH EXPERIMENT

We now turn to compare our numerical results with available experimental data.[6] The GaN/AlN QD structures con-

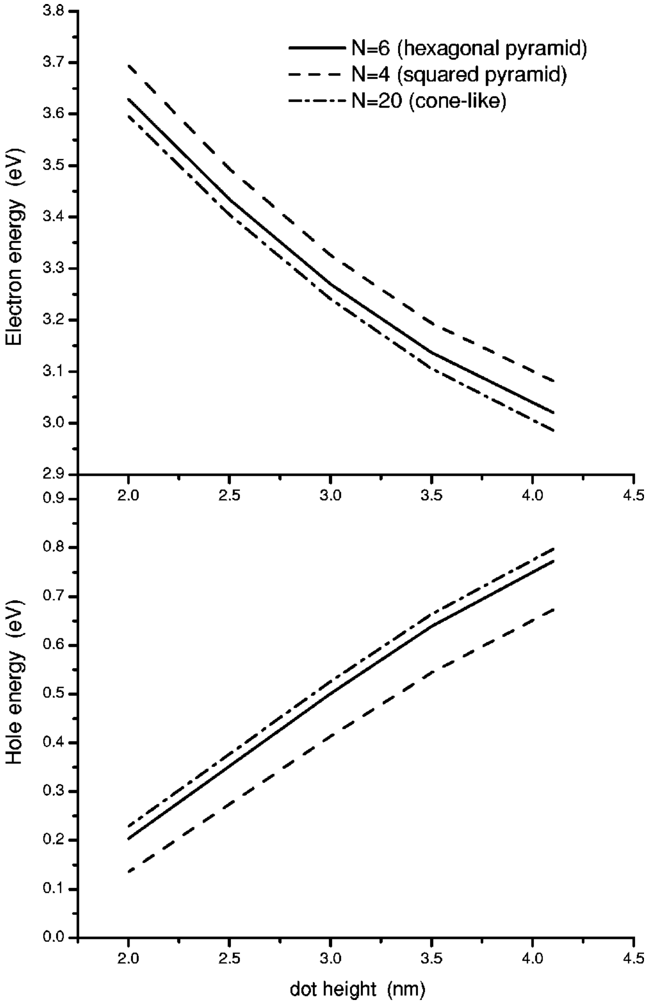

FIG. 10. Variation of (a) the electron and (b) hole ground-state energy level as a function of dot height, calculated for different QD shapes. Solid lines: hexagonal truncated pyramid ($N_{\rm corner}=6$), as shown in Fig. 1; dashed lines: square truncated pyramid ($N_{\rm corner}=4$); dot-dashed lines: 20-sided truncated pyramid ($N_{\rm corner}=20$), used to model a truncated cone. The zero of energy is set at the VB edge of bulk unstrained GaN. Material parameters used are listed in Tables I and II. The dot geometrical parameters vary with QD height as described in the text. The values of R_b, R_t, w, d_x, d_y, and d_z are the same for each shape for a given dot height h.

sidered in this section were chosen to be as close as possible to the structures grown and studied in Refs. 6, 24, and 47. Low-temperature photoluminescence (PL) spectra have been reported for two samples,[6] one with "large" QD's of height ≈4 nm, and the other with smaller dots, ≈2 nm high. The energies of the PL maximum in each of these two samples are shown by the filled circles in Fig. 11, along with the calculated dependence on QD size of the $E1$-$H1$ transition energy. The PL maximum for the large dot lies about 0.55 eV *below* the bandgap of bulk GaN, providing clear evidence for the strong built-in electric field in this QD structure. The transition energy for the large dot, calculated using the material parameters in Table I (solid line in Fig. 11), lies a further 200 meV lower, at about 2.75 eV. For "small" dots the calculated transition energy nearly coincides with that deduced from the experiment. Therefore we can conclude that the theoretical and experimental transition energies are in reasonable agreement, if we take account of the error bars for the experimental points. The calculated value of each transition energy depends, however, on the values assumed for the different material parameters used in the calculations. The energy levels of the carriers in the QD's are mainly determined by the strong built-in electric field. We therefore consider in more detail the influence of the assumed spontaneous polarization difference.

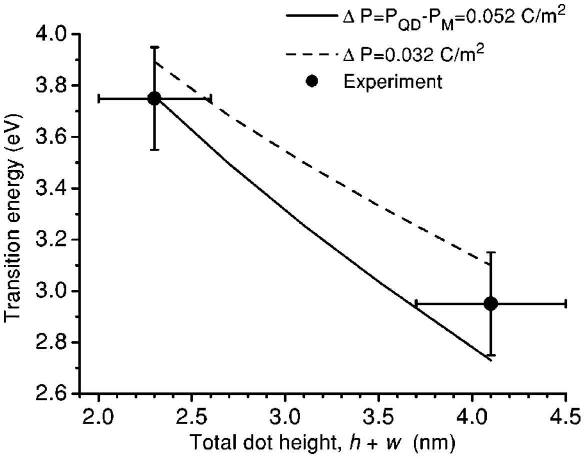

FIG. 11. Calculated dependence of the ground-state transition energy $E1$-$H1$ on the total QD height for different assumed values of the spontaneous polarization difference, $\Delta P_{\rm spont}=P_{\rm QD}-P_M$. Solid line: using the value of $\Delta P_{\rm spont}=0.052\,{\rm C/m^2}$ (Ref. 33) (see Table I); dashed line: $\Delta P_{\rm spont}=0.032\,{\rm C/m^2}$. The two solid circles with error bars are the experimental points from Ref. 6. Material parameters used (except for the spontaneous polarization) are given in Tables I and II. The dot geometry varies with QD height as follows: the wetting layer width is kept constant, $w=0.5$ nm; the QD height h is varied from 1.8 nm to 3.6 nm, the top diameter equals to the total QD height $2R_t=h+w$; the bottom diameter $2R_b$ varies linearly on the QD height from $R_b=8.5$ nm for a large dot of $h=3.6$ nm and $R_t=4.0$ nm for a small dot of $h=1.8$ nm.

The only values available for $P_{\rm spont}$ are those calculated by Bernardini, Fiorentini, and Vanderbilt.[33] These give the spontaneous polarization difference, which determines the contribution from the spontaneous polarization to the built-in electric field, as $\Delta P_{\rm spont}=0.052\,{\rm C/m^2}$ (see Table I). Assuming that this value is the upper limit for $\Delta P_{\rm spont}$, and to check the influence of $\Delta P_{\rm spont}$ on the carrier spectrum, we have also calculated the dependence of the transition energy on the QD size setting $\Delta P_{\rm spont}$ to 0.032 (dashed line in Fig. 11). This value is consistent with a previous analysis of the optical properties of GaN/AlGaN QW structures.[35] Leroux *et al.*[35] found that the best fit to the experimentally observed variation of PL peak energy with QW width was obtained for a series of GaN/Al$_{0.11}$G$_{0.89}$N QW's by assuming a built-in field of 450 kV/cm. This compares with the value of about 750 kV/cm predicted by Bernardini, Fiorentini, and Vanderbilt's[33] parameters (see Table I). The GaN QW's studied in Ref. 35 were found from x-ray measurements to be nearly relaxed. If we therefore assume that the built-in electric field is entirely due to the spontaneous polarization difference, we can estimate from the experimental data that $\Delta P_{\rm spont}=0.052\times 450/750=0.031\,({\rm C/m^2})$, suggesting that the spontaneous polarization values calculated by Bernardini, Fiorentini, and Vanderbilt may be overestimated. Other papers[59,60] have also concluded that the value of the spontaneous polarization difference should be less than that calculated in Ref. 33 and shown in Table I. In particular, a detailed analysis of experimental data on AlGaN/GaN QW's[59] demonstrated that the value of ΔP_{spont} is lower than that predicted by Bernardini, Fiorentini, and Vanderbilt,[33] as was also concluded from modeling of experimental results on AlGaN/GaN heterostructure field-effect transistors.[60] However, other recent experiments[61–63] have shown that the built-in electric fields calculated using Bernardini, Fiorentini, and Vanderbilt's parameters agree well with those deduced from experiment. Therefore some controversy remains related to the values of the spontaneous polarization constants. The transition energies for large GaN/AlN QD's calculated in this paper using the lower and upper values of ΔP_{spont} (0.032 dashed line in Fig. 11 and 0.052 C/m^2, solid line) are both consistent with the available experimental data, so that further data is required in order to determine more accurately the value of ΔP_{spont}. Finally we note that all calculations to data have assumed the magnitude of ΔP_{spont} to be independent of strain, and to vary linearly with composition, and likewise for the magnitude of the piezoelectric constants. Further work would be useful to confirm the accuracy of these assumptions.

VII. SUMMARY AND CONCLUSIONS

In summary, we have introduced in this paper an efficient method to calculate the strain and built-in electric-field distribution and the electronic structure of GaN/AlN QD structures, and then applied the technique to address a range of issues concerning such dot structures.

We first introduced an approach based on a Green's function tensor formalism to calculate the 3D strain distribution in QD structures of arbitrary shape, and with hexagonal (wurtzite) crystal symmetry. We presented a detailed derivation of an analytical expression for the Fourier transform of the QD strain tensor, valid for the case when the elastic constants of the QD and matrix materials are equal. We argued that this is normally a reasonable assumption for buried semiconductor quantum dots, but also outlined a simple iteration procedure that could treat the strain distribution in the case of unequal elastic constants. We obtain a compact analytical expression for the Fourier transform of the strain tensor. The 3D spatial distribution of the strain tensor is then found easily as the sum of the Fourier series.

We then used a similar technique to calculate the Fourier transform of the built-in electric field, including the strain-induced piezoelectric field and the contribution due to the spontaneous polarization. The two sets of field terms give approximately equal contributions to the calculated built-in electric field in GaN/AlN QD structures, where the overall electric field magnitude can be of the order of several MV/cm. For example, using the piezoelectric constants and spontaneous polarization values predicted by Bernardini, Fiorentini, and Vanderbilt,[33] we find the electric field in a GaN/AlN QD of height 4.1 nm to be around 6 MV/cm at the QD base and 4 MV/cm at the QD top. Such giant built-in electric fields are characteristic for GaN/AlN QD structures.

We next introduced an efficient technique to calculate the carrier energy spectrum and wave functions in a semiconductor heterostructure containing QD's of arbitrary shape. The method is a natural combination of the plane-wave expansion and Fourier-transform techniques used to derive the built-in strain and electric-field distributions. Each carrier wave function is expressed in a series expansion based on a suitable set of bulk states. The coefficients of the series and the carrier energy levels in any QD are then found as the eigenvectors and eigenvalues of a Hamiltonian matrix, all of whose matrix elements can be found analytically. The proposed technique does not require explicit calculation of the 3D spatial distribution of the built-in strain and electric fields. This makes the method effective and fast not only for spectrum calculations, but also for further modeling of the optical properties of the QD structures.

The built-in electric field has a crucial influence on the carrier states in GaN/AlN QD's. The electrons are pushed up to the QD top and holes are pushed down into the wetting layer below the QD. In addition, both electrons and holes experience a significant lateral confinement due to the built-in electrostatic potential. This creates an effective 3D potential for electrons and holes, with flat, circular symmetry. The form of the electron and hole wave functions in GaN/AlN QD's is therefore very similar to what would be expected for an infinitely deep flat cylinder. For the holes, the ground-state energy calculated using a one-band (effective-mass) Hamiltonian agreed well with that using a 3×3 valence-band Hamiltonian. By contrast, despite GaN being a wide-band-gap semiconductor, we found it essential to include conduction-band nonparabolicity effects when calculating the electron spectrum in GaN/AlN QD's. A one-band effective-mass Hamiltonian overestimated the electron ground-state energy by about 70–100 meV compared to the results of a 4×4 model, because of the strong vertical confinement due to the built-in electric field. We also briefly considered the influence of dot shape on the QD carrier spectrum, comparing a 6-sided and a 20-sided regular truncated pyramid (the latter structure is truncated conelike). The calculated ground-state energies were within 20 meV of each other, implying that our overall results and conclusions are generally insensitive to some uncertainties in the QD shape. Finally, the calculated dependence of the energy position of the first PL maximum on QD size is found to be in good agreement with two experimental points from Ref. 6 for ''large'' and ''small'' GaN/AlN QD's (heights respectively ~4.1 nm and 2.3 nm).

We conclude that the method introduced here gives valuable information on the electronic structure of GaN/AlN quantum dots, and should also be particularly convenient for a range of future studies, including modeling of optical transition rates, and laser gain characteristics of realistic quantum dot structures.

ACKNOWLEDGMENTS

This paper was partially supported by Brite/Euram project BE3381 (Rainbow). The visit of A.D.A. to the University of Surrey was supported by a grant from the Royal Society.

APPENDIX A: EFFECT OF DIFFERING ELASTIC CONSTANTS IN THE QD AND MATRIX MATERIALS

When the QD and matrix materials have different elastic constants, the elastic modulus tensor λ_{iklm} then depends on the space coordinate, and the Green's function satisfies the following equation:

$$\frac{\partial}{\partial x_k}\lambda_{iklm}(\mathbf{r})\frac{\partial}{\partial x_m}G_{\ln}(\mathbf{r},\mathbf{r}')=-\delta(\mathbf{r}-\mathbf{r}')\delta_{in}, \tag{A1}$$

where $\lambda_{iklm}(\mathbf{r})=\lambda^{\mathrm{QD}}_{iklm}\chi_{\mathrm{QD}}(\mathbf{r})+\lambda^{M}_{iklm}(\mathbf{r})[1-\chi_{\mathrm{QD}}(\mathbf{r})]$, and $\lambda^{\mathrm{QD}}_{iklm}$ and λ^{M}_{iklm} are the elastic tensors corresponding to the QD and matrix materials, respectively.

We outline here a method to find the Fourier transform of the elastic strain tensor for a single QD, $\tilde{e}^s_{ij}=\tilde{e}^{(0)}_{ij}+\tilde{e}^c_{ij}$, where the part e^c_{ij} of the total strain tensor is due to the displacement given by the second, integral term in Eq. (1) of Sec. II of this paper. The method is based on first determining a zeroth-order solution to Eq. (A1), similar to the solution presented in Sec. II. We then introduce an iterative technique that can be used to determine a converging series of corrections to the strain distribution.

We start with the Fourier transform of Eq. (A1) for the Green's tensor:

$$\begin{aligned}\lambda^{M}_{iklm}\xi_k\xi_m\tilde{G}_{\ln}(\boldsymbol{\xi},\mathbf{r}') &+(\delta\lambda)_{iklm}\xi_k\sum_{\tilde{\xi}}\tilde{\chi}_{\mathrm{QD}}(\boldsymbol{\xi}-\tilde{\boldsymbol{\xi}})\tilde{\xi}_m\tilde{G}_{\ln}(\tilde{\boldsymbol{\xi}},\mathbf{r}')\\ &=\frac{1}{(2\pi)^3}e^{-i\boldsymbol{\xi}\cdot\mathbf{r}'}\delta_{in},\end{aligned} \tag{A2}$$

where we introduce $(\delta\lambda)_{iklm}\equiv\lambda^{\mathrm{QD}}_{iklm}-\lambda^{M}_{iklm}$. In deriving Eq. (A2) we have used the following property of the Fourier transform, namely, that $\widetilde{f_1 f_2}=\Sigma_{\xi'}\tilde{f}_1(\boldsymbol{\xi}-\boldsymbol{\xi}')\tilde{f}_2(\boldsymbol{\xi}')$. Then, using Eqs. (1) and (A2) we obtain a set of linear equations for the strain components $\tilde{e}^c_{ij}$:

$$\begin{aligned}\lambda^{M}_{iklm}\xi_k\tilde{e}^c_m(\boldsymbol{\xi})&+(\delta\lambda)_{iklm}\xi_k\sum_{\tilde{\xi}}\tilde{\chi}_{\mathrm{QD}}(\boldsymbol{\xi}-\tilde{\boldsymbol{\xi}})\tilde{e}_{lm}(\tilde{\boldsymbol{\xi}})\\ &=-\lambda^{\mathrm{QD}}_{ikpr}e^T_{pr}\xi_k\tilde{\chi}_{\mathrm{QD}}(\boldsymbol{\xi}),\end{aligned} \tag{A3}$$

where $\lambda^{\mathrm{QD}}_{nkpr}e^T_{pr}$ is given by Eq. (9). This series of coupled integral equations for $\tilde{e}^c_{ij}$ can be solved numerically using standard techniques. However, it is more convenient to solve them using a variant of perturbation theory involving the following iterative procedure. In most cases of interest the values of the dot and matrix elastic constants are relatively close, so that $(\delta\lambda)/\lambda\ll 1$. The effect of a finite value of $\delta\lambda$ can then be considered using a perturbation series expansion. Let the strain tensor $\tilde{e}^c_{lm}$ be represented by the series

$$\tilde{e}^c_{lm}=\tilde{e}^{lm}_0+\tilde{e}^{lm}_1+\tilde{e}^{lm}_2+\cdots, \tag{A4}$$

where $\tilde{e}^{lm}_N\propto(\delta\lambda/\lambda)^N$. The convergence of the series in Eq. (A4) should be guaranteed since $(\delta\lambda)/\lambda\ll 1$. For the Nth term in Eq. (A4) we obtain the following set of equations:

$$\lambda^{M}_{iklm}\xi_k e^{lm}_N=F^{(N)}_i(\boldsymbol{\xi}), \tag{A5}$$

where

$$F^{(0)}_i(\boldsymbol{\xi})=-\lambda^{\mathrm{QD}}_{ikpr}e^T_{pr}\xi_k\tilde{\chi}_{\mathrm{QD}}(\boldsymbol{\xi}), \tag{A6}$$

$$E^{(m)}_i(\boldsymbol{\xi})=-(\delta\lambda)_{ikln}\xi_k\sum_{\tilde{\xi}}\tilde{\chi}_{\mathrm{QD}}(\boldsymbol{\xi}-\tilde{\boldsymbol{\xi}})e^{lm}_{N-1}(\tilde{\boldsymbol{\xi}}),\quad N>0. \tag{A7}$$

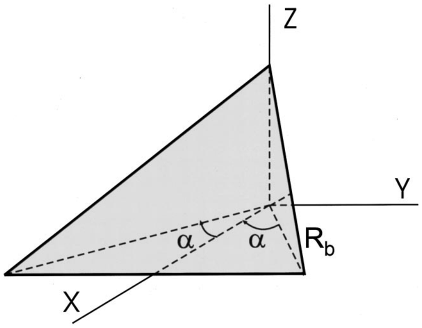

FIG. 12. Schematic view of the pyramid segment.

It can be shown that the linear system of equations described by Eq. (A5) has the following solution:

$$e^{lm}_N=\frac{(2\pi)^3}{2}[F^{(N)}_p(\boldsymbol{\xi})\xi_l G^N_{mp}(\boldsymbol{\xi})+F^{(N)}_p(\boldsymbol{\xi})\xi_m G^M_{lp}(\boldsymbol{\xi})], \tag{A8}$$

where G^M_{in} is the Green's tensor for the matrix material given by Eqs. (14), (21), and (22). Thus, application of Eqs. (A6) and (A8) provides an analytical route to evaluate a zeroth-order solution, e^{lm}_0, of the integral equation for $\tilde{e}^s_{ij}$ and also to determine higher-order corrections, e^{lm}_N, using the iterative scheme described above.

APPENDIX B: FOURIER TRANSFORM OF χ_{QD} FOR A TRUNCATED REGULAR *N*-SIDED PYRAMID

We derive here an analytical formula for the Fourier transform of the characteristic function $\chi_{\mathrm{QD}}(\mathbf{r})$ corresponding to a truncated regular N-sided pyramid. We first derive the Fourier transform for a single segment of a pyramid which has an N-sided polygonal base (see Fig. 12). The Fourier transform, $\chi_{\mathrm{QD}}(\boldsymbol{\xi})$, of the characteristic function of a general shape Ω is given by

$$\tilde{\chi}_{\mathrm{QD}}(\boldsymbol{\xi})=\frac{1}{(2\pi)^3}\int_{\Omega}e^{-i\boldsymbol{\xi}\cdot\mathbf{r}}\,dV. \tag{B1}$$

For the pyramid segment shown in Fig. 12 the integral (B1) has the form

$$\tilde{\chi}_{PS}=\int_0^{x_0}dx\,e^{-i\xi_x x}\int_{-y_0x/x_0}^{y_0x/x_0}dy\,e^{-i\xi_y y}\int_0^{h_{\mathrm{seg}}(1-x/x_0)}dz\,e^{-i\xi_z z}, \tag{B2}$$

where h_{seg} is the segment height, $x_0=R_b\cos\alpha$, $y_0=R_b\sin\alpha$, and for an N-sided pyramid $\alpha=\pi/N$. Evaluation of this integral is straightforward and gives

$$\tilde{\chi}_{PS} = -\frac{1}{\xi_y \xi_z}\left\{ I_e\left(x_0, -\xi_x - \xi_y \frac{y_0}{x_0} + \xi_z \frac{h_{\rm seg}}{x_0}\right) e^{-i\xi_z b_{\rm seg}} - I_e\left(x_0 - \xi_x + \xi_y \frac{y_0}{x_0} + \xi_z \frac{h_{\rm seg}}{x_0}\right) \times e^{-i\xi_x h_{\rm seg}} - I_e\left(x_0 - \xi_x - \xi_y \frac{y_0}{x_0}\right) + I_e\left(x_0, -\xi_x + \xi_y \frac{y_0}{x_0}\right)\right\}, \tag{B3}$$

where

$$I_e(a,b) = \int_0^a e^{ibx}\, dx = \frac{1}{ib}[e^{iba} - 1].$$

To find the Fourier transform of the pyramid we then use the principle of superposition and the fact that the Fourier transform of the volume $\tilde{V}$ (which is the image of volume V after coordinate transform $\mathbf{r} = T\tilde{\mathbf{r}}$, $\tilde{\mathbf{r}} = T^T \mathbf{r}$), is given by

$$F_V(\boldsymbol{\xi}) = F_{\tilde{V}}(\tilde{\boldsymbol{\xi}}), \tag{B4}$$

where $\tilde{\xi} = T^T \xi$. Thus, the Fourier transform of the N-sided pyramid, $\tilde{\chi}_{\rm pyr}(\boldsymbol{\xi})$ can be expressed as the superposition of N pyramid segments, each turned sequentially by an angle $2\pi/N$ around the z axis:

$$\tilde{\chi}_{\rm pyr}(\boldsymbol{\xi}) = \sum_{p=0}^{N-1} \tilde{\chi}_{PS}\left[\cos\left(\frac{2p\pi}{N}\right)\xi_1 + \sin\left(\frac{2p\pi}{N}\right)\xi_2, -\sin\left(\frac{2p\pi}{N}\right)\xi_1 + \cos\left(\frac{2p\pi}{N}\right)\xi_2, \xi_3\right]. \tag{B5}$$

Finally, the truncated pyramid can be regarded as the ''difference'' of two pyramids. The Fourier transform of the characteristic function of the truncated pyramid is therefore given by

$$\tilde{\chi}_{\rm QD}(\boldsymbol{\xi}) = \tilde{\chi}_{\rm pyr}(\boldsymbol{\xi}, R_b, h_l) - e^{-i\xi_z h}\tilde{\chi}_{\rm pyr}(\boldsymbol{\xi}, R_t, h_s), \tag{B6}$$

where the origin of the coordinate system is at the center of the QD base, R_b and R_t are the respective horizontal distances from the z axis to a bottom and top corner of the truncated pyramid, h is the height of the truncated pyramid and $\tilde{\chi}_{\rm pyr}(\boldsymbol{\xi}, R, h_{\rm pyr})$ is the Fourier transform for a pyramid with base segment size R and height $h_{\rm pyr}$, $h_s = R_t h/(R_b - R_t)$ and $h_l = R_b h/(R_b - R_t)$.

---

*On leave from A. F. Ioffe Physico-Technical Institute, 26 Polytekhnicheskaya, St. Petersburg 194021, Russia. Email address: a.andreev@surrey.ac.uk

[1] N. N. Ledentsov, V. M. Ustinov, V. A. Shchukin, P. S. Kopev, Z. I. Alferov, and D. Bimberg, Semiconductors **32**, 343 (1998).

[2] V. M. Ustinov, N. A. Maleev, A. E. Zhukov, A. R. Kovsh, A. Y. Egorov, A. V. Lunev, B. V. Volovik, I. L. Krestnikov, Y. G. Musikhin, N. A. Bert, P. S. Kopev, Z. I. Alferov, N. N. Ledentsov, and D. Bimberg, Appl. Phys. Lett. **74**, 2815 (1999).

[3] N. N. Ledentsov, V. A. Shchukin, M. Grundmann, N. Kirstaedter, J. Bohrer, O. Schmidt, D. Bimberg, V. M. Ustinov, A. Y. Egorov, A. E. Zhukov, P. S. Kopev, S. V. Zaitsev, N. Y. Gordeev, Z. I. Alferov, A. I. Borovkov, A. O. Kosogov, S. S. Ruvimov, P. Werner, U. Gosele, and J. Heydenreich, Phys. Rev. B **54**, 8743 (1996).

[4] J. H. Noh, H. Asahi, S. J. Kim, and S. Gonda, Jpn. J. Appl. Phys., Part 1 **36** (6B), 3818 (1997).

[5] K. Suzuki, R. A. Hogg, and Y. Arakawa, J. Appl. Phys. **85**, 8349 (1999).

[6] F. Widmann, J. Simon, D. Daudin, G. Feuillet, J. L. Rouviere, N. T. Pelekanos, and G. Fishman, Phys. Rev. B **58**, 15 989 (1998).

[7] K. Tachibana, T. Someya, and Y. Arakawa, Appl. Phys. Lett. **74**, 383 (1999).

[8] A. Petersson, A. Gustafsson, L. Samuelson, S. Tanaka, and Y. Aoyagi, Appl. Phys. Lett. **74**, 3513 (1999).

[9] J. Wang, M. Nozaki, M. Lachab, Y. Ishikawa, R. S. Qhalid Fareed, T. Wang, M. Hao, and S. Sakai, Appl. Phys. Lett. **75**, 950 (1999).

[10] S. Lee, I. Daruka, C. S. Kim, A. L. Barabasi, J. L. Merz, and J. K. Furdyna, Phys. Rev. Lett. **81**, 3479 (1998).

[11] A. D. Andreev, R. M. Datsiev, and R. P. Seisyan, Phys. Status Solidi B **215**, 325 (1999).

[12] M. Pinczolits, G. Springholz, and G. Bauer, Appl. Phys. Lett. **73**, 250 (1998).

[13] D. J. Eagleshman and M. Cerullo, Phys. Rev. Lett. **64**, 1943 (1990).

[14] M. Grundmann, O. Stier, and D. Bimberg, Phys. Rev. B **52**, 11 969 (1995).

[15] O. Stier, M. Grundmann, and D. Bimberg, Phys. Rev. B **59**, 5688 (1999).

[16] A. J. Williamson and A. Zunger, Phys. Rev. B **59**, 15 819 (1999).

[17] T. Benabbas, P. François, Y. Androussi, and A. Lefebvre, J. Appl. Phys. **80**, 2763 (1996).

[18] M. A. Cusack, P. R. Briddon, and M. Jaros, Phys. Rev. B **54**, R2300 (1996).

[19] J. R. Downes, D. A. Faux, and E. P. O'Reilly, J. Appl. Phys. **81**, 6700 (1997).

[20] A. D. Andreev, J. R. Downes, D. A. Faux, and E. P. O'Reilly, J. Appl. Phys. **86**, 297 (1999).

[21] A. D. Andreev and E. P. O'Reilly, in *Excitonic Processes in Condensed Matter*, edited by R. T. Williams and W. M. Yen, The Electrochemical Society Proceedings Series (Electrochemical Society, Pennington, NJ, 1998), Part 98, Vol. 25, pp. 271–280.

[22] J. D. Eshelby, Proc. R. Soc. London, Ser. A **241**, 376 (1957).

[23] I. M. Lifshits and L. N. Rosentsverg, Zh. Eksp. Teor. Fiz. **17**, 9 (1947) [in Russian]

[24] M. Arley, J. L. Rouviere, F. Widmann, B. Daudin, G. Feuillet, and H. Mariette, Appl. Phys. Lett. **74**, 3287 (1999).

[25] A. F. Wright, J. Appl. Phys. **82**, 2833 (1997).

[26] E. P. O'Reilly, Semicond. Sci. Technol. **2**, 121 (1989).

[27] K. Tsubouchi, K. Sugai, and N. Mikoshiba, in *1981 Ultrasonics Symposium*, edited by B. R. McAvoy (IEEE, New York, 1981), Vol. 1, p. 375.

[28] L. E. McNeil, M. Grimsditch, and R. H. French, J. Am. Ceram. Soc. **76**, 1132 (1993).

[29] A. U. Sheleg and V. A. Savastenko, Izv. Akad Nauk SSSR, Neorg. Mater. **15**, 1598 (1979).

[30] A. Polian, M. Grimsditch, and I. Grzegory, J. Appl. Phys. **79**, 3343 (1996).

[31] R. W. Keyes, J. Appl. Phys. **33**, 3371 (1962).

[32] A. D. Prins and D. J. Dunstan, Philos. Mag. Lett. **58**, 37 (1988).

[33] F. Bernardini, V. Fiorentini, and D. Vanderbilt, Phys. Rev. B **56**, R10 024 (1997).

[34] V. Fiorentini, F. Bernardini, F. D. Sala, A. D. Carlo, and P. Lugli, cond-mat/9808098, 1999.

[35] M. Leroux, N. Grandjean, M. Laugt, J. Massies, B. Gil, P. Lefebvre, and P. Bigenwald, Phys. Rev. B **58**, R13 371 (1998).

[36] N. Grandjean, M. Leroux, and J. Massies, Appl. Phys. Lett. **74**, 2361 (1999).

[37] Landolt-Bornstein, *Numerical Data and Functional Relationships in Science and Technology*, edited by O. Madelung (Springer-Verlag, Berlin, 1982), Vol. III, p. 17b.

[38] A. L. Efros and M. Rosen, Phys. Rev. B **58**, 7120 (1998).

[39] A. D. Andreev and A. A. Lipovskii, Phys. Rev. B **59**, 15 402 (1999).

[40] A. D. Andreev and R. A. Suris, Semiconductors **30**, 285 (1996).

[41] P. W. Fry, I. E. Itskevich, D. J. Mowbray, M. S. Skolnick, J. A. Barker, E. P. O'Reilly, L. R. Wilson, I. A. Larkin, P. A. Maksym, M. Hopkinson, M. Al-Khafaji, J. P. R. Davis, A. G. Cullis, G. Hill, and J. C. Clark, Phys. Rev. Lett. **84**, 733 (2000).

[42] J. A. Barker and E. P. O'Reilly, Phys. Rev. B **61**, 13 840 (2000).

[43] A. D. Andreev and E. P. O'Reilly, in *GaN and Related Alloys*, edited by S. J. Pearton, C. Kuo, T. Uenoyama, and A. F. Wright, MRS Symposia Proceedings No. 537 (Materials Research Society, Pittsburgh, 1999).

[44] A. D. Andreev, Proc. SPIE **3284**, 151 (1998).

[45] N. Grandjean, J. Massies, and O. Tottereau, Phys. Rev. B **55**, 10 189 (1997).

[46] C. Priester and M. Lanoo, Appl. Surf. Sci. **123**, 658 (1998).

[47] F. Widmann, B. Daudin, G. Feuillet, Y. Samson, J. L. Ruviere, and N. Pelekanos, J. Appl. Phys. **83**, 7618 (1998).

[48] Y. C. Yeo, T. C. Chang, and M. F. Li, J. Appl. Phys. **83**, 1429 (1998).

[49] S. L. Chuang and C. S. Chang, Phys. Rev. B **54**, 2491 (1996).

[50] M. Kumagi, S. L. Chuang, and H. Ando, Phys. Rev. B **57**, 15 303 (1998).

[51] S. K. Pugh, D. J. Dugdale, S. Brand, and R. A. Abram, Semicond. Sci. Technol. **14**, 23 (1999).

[52] T. C. Chong, Y. C. Yeo, M. F. Li, and W. J. Fan, in *Nitride Semiconductors*, edited by F. A. Pence, S. P. De Baars, B. K. Meyer, I. C. Nakamura, and S. Btrite, MRS Symposia Proceedings No. 482 (Materials Research, Society, Pittsburgh, 1998), p. 67.

[53] J. Baur, K. Maier, M. Kunzer, U. Kaufmann, and J. Schneider, Appl. Phys. Lett. **65**, 2211 (1994).

[54] S. W. King, C. Ronning, R. F. Davis, M. C. Benjamin, and R. J. Nemanich, J. Appl. Phys. **84**, 2086 (1998).

[55] Z. Sitar, M. J. Paisley, B. Yabn, R. F. Davis, J. Ruan, and J. W. Choyke, Thin Solid Films **200**, 311 (1991).

[56] J. R. Waldrop and R. W. Grant, Appl. Phys. Lett. **68**, 2879 (1996).

[57] D. F. Nelson, R. C. Miller, and D. A. Kleinman, Phys. Rev. B **35**, 7770 (1987).

[58] A. T. Meney, B. Gonul, and E. P. O'Reilly, Phys. Rev. B **50**, 10 893 (1994).

[59] N. Grandjean, B. Damilano, S. Dalmasso, M. Leroux, M. Laugt, and J. Massies, J. Appl. Phys. **86**, 3714 (1999).

[60] J. A. Garrido, J. L. Sanchez-Rojas, A. Jimenez, E. Munoz, F. Omnes, and P. Gibart, Appl. Phys. Lett. **75**, 2407 (1999).

[61] O. Ambacher, B. Foutz, J. Smart, J. R. Shealy, N. G. Weimann, K. Chu, M. Murphy, A. J. Sierakowski, W. J. Schaff, L. F. Eastman, R. Dimitrov, A. Mitchell, and M. Stutzmann, J. Appl. Phys. **87**, 334 (2000).

[62] R. Langer, J. Simon, V. Ortiz, N. T. Pelekanos, A. Barski, R. Andre, and M. Godlewski, Appl. Phys. Lett. **74**, 3827 (1999).

[63] J. Simon, R. Langer, A. Barski, and N. T. Pelekanos, Phys. Rev. B **61**, 7211 (2000).